Polyhedron 212 (2022) 115577

Contents lists available at ScienceDirect

Polyhedron

journal homepage: www.elsevier.com/locate/poly

Structural speciation in chemical reactivity profiling of binary-ternary systems of Ni(II) with iminodialcohol and aromatic chelators

S. Matsia [a], A. Kaoulla [a], M. Menelaou [a,e], A. Hatzidimitriou [b], T. Papadopoulos [c], M. K. Reimann [d], R. Pöttgen [d], A. Salifoglou [a,*]

[a] Laboratory of Inorganic Chemistry and Advanced Materials, School of Chemical Engineering, Aristotle University of Thessaloniki, Thessaloniki 54124, Greece
[b] Laboratory of Inorganic Chemistry, School of Chemistry, Aristotle University of Thessaloniki, Thessaloniki 54124, Greece
[c] Department of Mathematical and Physical Sciences, Thornton Science Park, University of Chester, Chester CH2 4NU, UK
[d] Institut für Anorganische und Analytische Chemie, Universität Münster, Corrensstrasse 30, Münster D-48149, Germany
[e] Department of Chemical Engineering, Faculty of Geotechnical Sciences and Environmental Management, Cyprus University of Technology, Limassol 3036, Cyprus

ARTICLE INFO

Keywords:
Nickel complex synthesis
Iminodialcohol ligand
Structure elucidation
Magnetic properties
Chemical reactivity patterns

ABSTRACT

The importance of structural speciation in the control of chemical reactivity in Ni(II) binary-ternary systems, involving (O,O,N)-containing substrates (1,1′-iminodi-2-propanol), and aromatic chelators (2,2′-bipyridine, 1,10-phenanthroline), prompted the systematic synthesis of new crystalline materials characterized by elemental analysis, FT-IR, UV-Visible, Luminescence, magnetic susceptibility, and X-ray crystallography. The structures contain mononuclear octahedral assemblies, the lattice architecture of which exemplifies reaction conditions under which conformational variants and solvent-associated lattice-imposed complexes are assembled. Transformations between complex species denote their association with reactivity pathways, suggesting alternate synthetic methodologies for their isolation. Theoretical work (Hirshfeld, Electrostatic Potential, DFT) signifies the impact of crystal structure on energy profiles of the generated species. The arisen physicochemical profiles of all compounds portray a well-configured interwoven network of pathways, projecting strong connection between structural speciation and Ni(II) reactivity patterns in organic-solvent media. The collective results provide well-defined parameterized profiles, poised to influence the synthesis of new Ni(II)-iminodialcohol materials with specified structural-magneto-optical properties.

1. Introduction

Chemical reactivity and structural diversity of coordination compounds play a central role in the design and synthesis of new material assemblies. Through such assemblies, transition metal(II,III) ions emerge as extremely important components in abiotic systems, such as electronics, magnetics, catalysis, optics, advanced corrosion resistant materials, and others [1–3]. Among them, Ni(II) is often encountered in both abiotic and biological systems. Nickel has been identified as a micronutrient and microbial growth inhibitor [4]. Beyond any application, however, introduction of such an element in hybrid systems contributes to the formulation of its physical and chemical properties, so as to project novel roles in complex processes, including catalytic transformations. In the case of biological systems, Ni(II) as a metal cofactor [5], plays an important role in metalloenzymes [6–8]. In that sense, the chemical and electronic properties of nickel, in its ordinary oxidation state Ni(II), bring out noticeable attributes of new materials, exemplifying among others magnetism and magnetic identity.

In the chemistry of metal-organic assemblies, considerable attention over the past few years has focused on organic linkers, especially those with N- and/or O-containing terminals, which can act as anchors to or bridging ligands between metal ion centers, thus promoting diversity in architecture assemblies [9,10]. As multidentate ligands, amino-alcohols, with well-defined terminal (N,O,O)-containing anchors, are such ligands, capable of promoting metal ion chemical reactivity [11]. That reactivity results in metal ion binding, often with metallacyclic rings bestowing enhanced stability upon the arising metal-organic assemblies. These organic ligands have also been amply encountered in biological systems and abiotic materials linked to diverse chemical and magnetic properties. A distinct member of that family of ligands, capable of functioning as a metal-organic binder, is 1,1′-imino-2-dipropanol (Imino), which bears both oxygen and sp^3 nitrogen anchors poised to

* Corresponding author.
E-mail address: salif@auth.gr (A. Salifoglou).

https://doi.org/10.1016/j.poly.2021.115577
Received 1 August 2021; Accepted 3 November 2021
Available online 10 November 2021

seek metal ion chelation in a multitude of ways. In so doing, the aforementioned structural features preempt its use in the synthesis of new metal complex materials with distinct structural and spectroscopic properties.

Given, therefore, the a) importance of the structure of amino-alcohol ligands in dictating metal ion binding reactivity toward Ni(II), thus giving rise to hybrid coordination complex materials of distinct coordination geometry, composition, and properties, and b) paucity of well-defined binary and ternary materials of Ni(II) with amino alcohols, reflecting clear correlations between structural speciation and reactivity pathways at both levels, Ni(II):1,1′-imino-2-dipropanol systems were investigated synthetically in alcoholic media, in the presence of aromatic chelators (2,2′-bipyridine; bipy, 1,10-phenanthroline; phen) as ternary ancillary ligands. The newly emerging materials, albeit seemingly simplistic in their composition and structure, possess distinctly differentiated physicochemical properties, thus allowing through a) uniquely defined reaction conditions, and b) ligand-specific transformation chemistry, the experimentally and theoretically supported formulation of chemical reactivity profiles that could assist in the future design and synthesis of Ni(II):Imino-containing materials of specified structural, electronic, and magnetic properties.

2. Experimental section

2.1. Materials and methods

All manipulations were carried out under aerobic conditions. The following starting materials were used without further purification: Nickel nitrate hexahydrate $Ni(NO_3)_2{\cdot}6H_2O$ was purchased from J.T. Baker and Carlo Erba, 1,1′-iminodi-2-propanol (H_3L or Imino) from Merck-Schuchardt and 2,2′-Bipyridine (bipy) from Panreac. 1,10-phenanthroline (phen) as well as solvents (acetonitrile, methanol) were supplied by Sigma Aldrich. Diethyl ether was purchased from Honeywell.

2.2. Physical measurements

FT-IR spectra were recorded on a ThermoFinnigan FT-Infra Red 200 spectrometer, using KBr pellets. UV/Visible measurements were carried out on a Hitachi U2001 spectrophotometer in the range from 190 to 1100 nm with a scan speed of 1200 nm/min. Spectral fitting of solutions in all compounds investigated in methanol was pursued by using the SYSTAT software Inc. Peakfit program (Version 4.11) (Supplementary Information). A Thermo Finnigan Flash EA 1112 CHNS elemental analyser was used for the simultaneous determination of carbon, hydrogen, and nitrogen (%). The analyser operation is based on the dynamic flash combustion of the sample (at 1800 °C) followed by reduction, trapping, complete GC separation and detection of the products. The instrument is a) fully automated and controlled by PC via the Eager 300 dedicated software, and b) capable of handling solid, liquid or gaseous substances.

2.3. Magnetic susceptibility

The polycrystalline powders (between 8 and 16 mg total sample mass) on all investigated compound samples were introducted into polypropylene capsules and attached to the sample holder rod of a Vibrating Sample Magnetometer (VSM) option of a Physical Property Measurement System (PPMS) by Quantum Design. Magnetization data M(T,H) of the samples were collected in a temperature range from 2.5 to 300 K, with applied fields of up to 60 kOe. The temperature dependence of the magnetic susceptibility was first recorded with an external field of 1 kOe over the entire temperature range. In the low-temperature region, we subsequently collected data in the field-cooled (ZFC) mode at 20 or 50 Oe. Magnetization isotherms were all recorded at 3 K. The experimental susceptibilities were corrected for core diamagnetism using the tabulated values by Bain and Berry [12,13].

2.4. Photoluminescence

Solid-state emission and excitation spectra (200–900 nm) were recorded on a Hitachi F-7000 fluorescence spectrophotometer from Hitachi High-Technologies Corporation. The employed split widths (em, ex) were 5.0 nm and the scan speed was 1200 $nm{\cdot}min^{-1}$. All measurements were carried out at room temperature. The entire system was supported by the appropriate computer software, FL Solutions 2.1, running on Windows XP.

2.5. Theoretical calculations

Bond Valence Sum (BVS) calculations were carried out using the Visualization for Electronic and Structural Analysis (VESTA) program (Version 3.4.8) [14]. Bond valence values (S) were obtained using the empirical expression $S = \exp[(R_o - r)/b]$, where $b = 0.37$ Å, r is the observed bond length and R_o (Å) is a tabulated constant. In our case, literature [15,16] R_o values are as follows: Ni(II)-O 1.654 and Ni(II)-N 1.647.

2.6. Hirshfeld surface analysis

The presence of various intermolecular interactions and the charge distribution in compounds **1**–**8** were investigated through Hirshfeld and electrostatic potential surface analysis [17–19]. Hirshfeld analysis (mapped over d_e, d_i, and/or d_{norm}), the electrostatic potential, and two-dimensional (2D) fingerprint [20–22] plots were calculated using Crystal Explorer [23], with bond lengths to hydrogen atoms set to standard values [24]. The wavefunction generating the electrostatic potential surface was obtained through the *Tonto* computational package, using the B3LYP correlation function and 6-31G(d,p) basis set over a range 0.05 a.u. During mapping, the derived surfaces were kept transparent for the visualization of various intermolecular interactions associated with self-assembly.

Hirshfeld surface plots, encompassing a) interactions from the internal surface to the nearest atom center of an outer molecule (d_i), b) contacts from the nearest molecules to the investigated surface (d_e), and/or c) the combination of internal and external distances, normalized by Van der Waals radius (d_{norm}), are displayed through colored graphics. Red color indicates shorter intermolecular contacts, white color reflects contacts around the r^{vdw} separation, and blue color indicates longer contact distances [25]. Assignment of intermolecular contacts and specific types of interactions can be highlighted in resolved fingerprint plots [20,21,22], as projections of mapped surfaces. Additional information can be revealed through blue-red electrostatic potential mapping, thus pointing out the donor-acceptor regions of the investigated surfaces [26,27].

2.7. Computational analysis

The Vienna Ab Initio Simulation Package (VASP), version 5.3.3 [28], was employed in order to study the electronic structure of all Ni-complex assemblies using Density Functional Theory (DFT). The Perdew-Burke-Ernzerhof (PBE) gradient-corrected exchange-correlation functional [29] was used and calculations were performed using plane-wave basis sets, and the projector augmented wave (PAW) method, with a plane-wave cut-off energy of 400 eV. In addition, a Γ centered k-point grid of 5×5×5 was employed for all calculations related to electronic structure for complex **1A**, 8×8×2 for complex **1B**, 6×4×2 for complex **2**, 8×4×3 for complex **3**, 8×8×4 for complex **6**, and 8×2×8 for complex **7**, whereas a 2×2×2 k-point grid was used for all isolated compounds. The tetrahedron method with Blöchl corrections and a smearing width of 0.1 eV were used to determine how partial occupancies are set for each wave function. Initial crystal structure and atomic coordinates were taken from the available crystallographic data (vide infra).

3. Synthesis and chemical transformations

3.1. Synthesis

Synthesis of $[Ni(C_6H_{15}NO_2)_2](NO_3)_2 \bullet CH_3CN\bullet H_2O$ (**1**). $Ni(NO_3)_2{\cdot}6H_2O$ (0.58 g, 2.0 mmol) was added in a 50 mL round bottom flask, in 10 mL of acetonitrile, under continuous stirring. Next, 1,1′-iminodi-2-propanol (0.54 g, 4.0 mmol) was added into the emerging green solution. The reaction mixture was then stirred for 10 min at room temperature and the reaction solution was filtered and layered with diethyl ether. After five days, at 4 °C, green prismatic crystals grew out of solution. The product was isolated by filtration and dried in vacuo. Yield: 0.48 g (~47 %). Anal. Calc. for **1**, ($C_{14}H_{35}N_5NiO_{11}$ MW = 508.17): C, 33.06; H, 6.89; N, 13.77. Found: C, 32.98; H, 6.85; N, 13.78.

Synthesis of $[Ni(C_6H_{15}NO_2)_2](NO_3)_2$ (**2**). $Ni(NO_3)_2{\cdot}6H_2O$ (0.58 g, 2.0 mmol) was added in a 50 mL round bottom flask, containing 8 mL of acetonitrile, under continuous stirring. Next, 1,1′-iminodi-2-propanol (0.52 g, 4.0 mmol) was placed in 2 mL of acetonitrile and the resulting solution was added slowly to the emerging green solution. The reaction mixture was then stirred for 10 min at room temperature and the reaction solution was filtered and layered with diethyl ether. After one week, at 4 °C, green prismatic crystals grew out of solution. The product was isolated by filtration and dried in vacuo. Yield: 0.48 g (~54 %). Anal. Calc. for **2**, ($C_{12}H_{30}N_4NiO_{10}$ MW = 449.10): C, 32.09; H, 6.73; N, 12.48. Found: C, 32.14; H, 6.70; N, 12.52.

Synthesis of $[Ni(C_6H_{15}NO_2)(C_{10}H_8N_2)(NO_3)](NO_3) \bullet 0.25CH_3OH$ (**3**). $Ni(NO_3)_2{\cdot}6H_2O$ (0.29 g, 1.0 mmol) was added in a 50 mL round bottom flask, containing 8 mL of methanol, under continuous stirring. Next, 1,1′-iminodi-2-propanol (0.13 g, 1.0 mmol) was placed in 2 mL of methanol and the solution was added slowly to the emerging green solution. The resulting light blue reaction mixture was stirred at room temperature for 10 min. Subsequently, bipy (0.16 g, 1.0 mmol) was added slowly to the reaction mixture under continuous stirring. The emerging reaction mixture was filtered and layered with diethyl ether. After one and a half months, at 4 °C, green prismatic crystals grew out of solution. The product was isolated by filtration and dried in vacuo. Yield: 0.29 g (~61 %). Anal. Calc. for **3**, ($C_{16.25}H_{24}N_5NiO_{8.25}$ MW = 480.11): C, 40.62; H, 5.00; N, 14.58. Found: C, 40.54; H, 4.96; N, 14.62.

Synthesis of $[Ni(C_6H_{15}NO_2)(C_{12}H_8N_2)(NO_3)](NO_3) \bullet CH_3OH$ (**4**). $Ni(NO_3)_2{\cdot}6H_2O$ (0.29 g, 1.0 mmol) was dissolved in 8 mL of methanol, in a 50 mL round bottom flask, under continuous stirring. To that, a solution of 1,1′-iminodi-2-propanol (0.13 g, 1.0 mmol) in 2 mL of methanol was added. The light blue reaction mixture was then stirred at room temperature for 10 min. Next, phen (0.18 g, 1.0 mmol) was added slowly to the reaction mixture under continuous stirring. Subsequently, the emerging reaction solution was filtered and layered with diethyl ether. After one month at 4 °C, blue crystalline plates grew out of solution. The product was isolated by filtration and dried in vacuo. Yield: 0.24 g (~45 %). Anal. Calc. for **4**, ($C_{19}H_{27}N_5NiO_9$ MW = 528.16): C, 43.18; H, 5.11; N, 13.26. Found: C, 43.21; H, 5.08; N, 13.30.

Synthesis of $[Ni(C_{10}H_8N_2)(NO_3)(CH_3CN)(H_2O)_2](NO_3)$ (**5**). $Ni(NO_3)_2{\cdot}6H_2O$ (0.29 g, 1.0 mmol) was dissolved in 10 mL of acetonitrile, in a 50 mL round bottom flask, under continuous stirring. Next, bipy (0.16 g, 1.0 mmol) was added slowly under continuous stirring. The blue reaction mixture was then stirred at room temperature for 10 min. Subsequently, the emerging reaction solution was filtered, and layered with diethyl ether. After a day or so, at 4 °C, light blue plates grew out of solution. The product was isolated by filtration and dried in vacuo. Yield: 0.21 g (~51 %). Anal. Calc. for **5**, ($C_{12}H_{15}N_5NiO_8$ MW = 415.99): C, 34.62; H, 3.61; N, 16.83. Found: C, 34.56; H, 3.58; N, 16.78.

Synthesis of $[Ni(C_{12}H_8N_2)_2(NO_3)(CH_3OH)](NO_3)$ (**6**). $Ni(NO_3)_2{\cdot}6H_2O$ (0.29 g, 1.0 mmol) was dissolved in 10 mL of methanol, in a 50 mL round bottom flask, under continuous stirring. To that, phen (0.36 g, 2.0 mmol) was added under stirring. The purple reaction mixture was then stirred at room temperature for 5 min. The final reaction solution was filtered, and layered with diethyl ether. After a day or so, at 4 °C, violet prismatic crystals grew out of solution. The product was isolated by filtration and dried in vacuo. Yield: 0.20 g (35 %). Anal. Calc. for **6**, ($C_{25}H_{20}N_6NiO_7$ MW = 575.18): C, 52.16; H, 3.48; N, 14.60. Found: C, 52.11; H, 3.44; N, 14.55.

Synthesis of $[Ni(C_{12}H_8N_2)_2(NO_3)(CH_3OH)](NO_3)$ (**7**). $Ni(NO_3)_2{\cdot}6H_2O$ (0.29 g, 1.0 mmol) was dissolved in 10 mL of methanol, in a 50 mL round bottom flask, under continuous stirring. To that, phen (0.54 g, 3.0 mmol) was added slowly and under stirring. The purple solution was stirred for 5 min at room temperature, filtered, and layered with diethyl ether. Three days later, at 4 °C, green prismatic crystals grew out of the solution. The product was isolated by filtration and dried in vacuo. Yield: 0.18 g (32 %). Anal. Calc. for **7**, ($C_{25}H_{20}N_6NiO_7$ MW = 575.18): C, 52.16; H, 3.48; N, 14.60. Found: C, 52.18; H, 3.46; N, 14.62.

Synthesis of $\{[Ni(C_{12}H_8N_2)_3]_2[Ni(H_2O)_6]\}(NO_3)_6 \bullet 4CH_3CN\bullet H_2O$ (**8**). $Ni(NO_3)_2{\cdot}6H_2O$ (0.29 g, 1.0 mmol) was dissolved in 10 mL of acetonitrile, in a 50 mL round bottom flask, under continuous stirring. To that, phen (0.36 g, 2.0 mmol) was added slowly and under stirring. The purple solution was stirred for 5 min at room temperature, filtered, and layered with diethyl ether. After a day or so, at 4 °C, pink prismatic crystals grew out of solution. The product was isolated by filtration and dried in vacuo. Yield: 0.52 g (~27 %). Anal. Calc. for **8**, ($C_{80}H_{74}N_{22}Ni_3O_{25}$ MW = 1919.73): C, 50.00; H, 3.85; N, 16.04. Found: C, 49.94; H, 3.87; N, 16.01.

3.2. Transformations

Transformation of $[Ni(C_6H_{15}NO_2)_2](NO_3)_2$ (**2**) to $[Ni(C_6H_{15}NO_2)(C_{10}H_8N_2)(NO_3)](NO_3) \bullet 0.25CH_3OH$ (**3**). $[Ni(C_6H_{15}NO_2)_2](NO_3)_2$ (0.45 g, 1.0 mmol) was dissolved in 10 mL of methanol, in a 50 mL round flask, under continuous stirring for 15 min. Next, bipy (0.16 g, 1.0 mmol) was added to the reaction mixture under stirring. The resulting dark blue solution was stirred for 10 min at room temperature, filtered, and layered with diethyl ether. After one month, at 4 °C, green prismatic crystals grew out of solution. The product was isolated by filtration and dried in vacuo. Yield: 0.13 g (27 %). The material was further identified and characterized as **3** by FT-IR and single crystal X-ray crystallography.

Transformation of $[Ni(C_6H_{15}NO_2)_2](NO_3)_2$ (**2**) to $[Ni(C_6H_{15}NO_2)(C_{12}H_8N_2)(NO_3)](NO_3) \bullet CH_3OH$ (**4**). $[Ni(C_6H_{15}NO_2)_2](NO_3)_2$ (0.14 g, 0.31 mmol) was dissolved in 7.5 mL of methanol, in a 50 mL round flask, under continuous stirring for 15 min. Next, phen (0.060 g, 0.33 mmol) was added to the reaction mixture. The resulting blue solution was stirred for 10 min at room temperature, filtered, and layered with diethyl ether. After one month, at 4 °C, blue plates grew out of solution. The product was isolated by filtration and dried in vacuo. Yield: 0.12 g (73 %). The material was further confirmed as **4** by FT-IR and single crystal X-ray crystallography.

Transformation of $[Ni(C_6H_{15}NO_2)_2](NO_3)_2$ (**2**) to $[Ni(C_6H_{15}NO_2)(C_{12}H_8N_2)(NO_3)](NO_3) \bullet CH_3OH$ (**4**). $[Ni(C_6H_{15}NO_2)_2](NO_3)_2$ (0.51 g, 1.1 mmol) was added in a 50 mL round bottom flask, in 8.5 mL of methanol, under continuous stirring. To that, phen (0.36 g, 2.0 mmol) was added to the reaction mixture. The resulting purple solution was stirred for 10 min at room temperature, filtered, and layered with diethyl ether. After one month, at 4 °C, blue plates grew out of the solution. The product was isolated by filtration and dried in vacuo. Yield: 0.15 g (25 %). The material was further confirmed as **4** by FT-IR and X-ray Crystallography.

3.3. X-ray crystal structure determination

Single crystals of compounds **1**–**8** were obtained from reaction mixtures according to the described synthetic procedures. For the structural determination of **1**–**8**, single crystals of the respective compounds were mounted on a Bruker Kappa APEX II diffractometer,

equipped with a triumph monochromator at ambient temperature. Diffraction measurements were recorded using Mo Kα radiation. Unit cell dimensions were determined by using at least 100 reflections in the range $15< \theta <20^{\circ}$. Intensity data were collected using φ and ω scan modes. The frames collected for each crystal were integrated with the Bruker SAINT software package [30], using a narrow-frame algorithm. Data were corrected for absorption using the numerical method (SADABS) based on crystal dimensions [31].

All structures were solved using the SUPERFLIP [32] package and refined by full–matrix least-squares method on F^2, using the CRYSTALS package version 14.61_build_6236 [33]. All non-disordered non-hydrogen atoms have been refined anisotropically.

All hydrogen atoms were found at their expected positions and refined using soft constraints. By the end of the refinement, they were positioned using riding constraints. The crystal data, details of data collection and structure refinement for all compounds studied are given in Table 1. Illustrations were drawn by Mercury [34] and Diamond [35]. Further details on the crystallographic studies as well as atomic displacement parameters are given as Supporting Information in the form of cif files.

4. Results

4.1. Synthetic procedures

Chemical reactivity investigation of the divalent metal ion Ni(II), in the presence of the (imino)alcohol ligand (1,1′-iminodi-2-propanol) and N,N'-chelators (bipy, phen), led to the synthesis and isolation of binary and ternary crystalline materials **1**–**8** in the solid state. The expeditious reactions in the aforementioned systems were carried out under variable molar ratios of the employed reagents, in both methanol and acetonitrile. Potential diversification of the structural speciation of Ni(II) was investigated through employment of different aromatic chelators. Specifically:

Green crystalline compound $[Ni(C_6H_{15}NO_2)_2](NO_3)_2 \bullet CH_3CN \bullet H_2O$ (**1**) was synthesized through a reaction of $Ni(NO_3)_2{\cdot}6H_2O$ and 1,1′-iminodi-2-propanol (Imino), with a 1:2 molar ratio, at 25 °C, using acetonitrile as a solvent. The overall stoichiometric reaction leading to **1** is shown below:

Table 1
Summary of crystallographic data on compounds $[Ni(C_6H_{15}NO_2)_2](NO_3)_2 \bullet CH_3CN \bullet H_2O$ (**1**), $[Ni(C_6H_{15}NO_2)_2](NO_3)_2$ (**2**), $[Ni(C_6H_{15}NO_2)(C_{10}H_8N_2)(NO_3)](NO_3) \bullet 0.25CH_3OH$ (**3**), $[Ni(C_6H_{15}NO_2)(C_{12}H_8N_2)(NO_3)](NO_3) \bullet CH_3OH$ (**4**), $[Ni(C_{10}H_8N_2)(NO_3)(CH_3CN)(H_2O)_2](NO_3)$ (**5**), $[Ni(C_{12}H_8N_2)_2(NO_3)(CH_3OH)](NO_3)$ (**6**), $[Ni(C_{12}H_8N_2)_2(NO_3)(CH_3OH)](NO_3)$ (**7**), $\{[Ni(C_{12}H_8N_2)_3]_2[Ni(H_2O)_6]\}(NO_3)_6 \bullet 4CH_3CN \bullet H_2O$ (**8**).

Compound	1	2	3	4	5	6	7	8
Chemical formula	$C_{14}H_{35}N_5NiO_{11}$	$C_{12}H_{30}N_4NiO_{10}$	$C_{16.25}H_{24}N_5NiO_{8.25}$	$C_{19}H_{27}N_5NiO_9$	$C_{12}H_{15}N_5NiO_8$	$C_{25}H_{20}N_6NiO_7$	$C_{25}H_{20}N_6NiO_7$	$C_{80}H_{74}N_{22}Ni_3O_{25}$
M_r	508.17	449.10	480.11	528.16	415.99	575.18	575.18	1919.73
Crystal system	Triclinic	Tetragonal	Monoclinic	Triclinic	Triclinic	Triclinic	Monoclinic	Triclinic
Space group	$P\bar{1}$	$P\bar{4}\,2_1c$	$P2_1/n$	$P\bar{1}$	$P\bar{1}$	$P\bar{1}$	$P2_1/c$	$P\bar{1}$
Temperature (K)	295	295	295	295	295	295	295	295
a (Å)	11.2159(7)	11.8454(2)	7.861(3)	7.9010(11)	7.3152(11)	8.2968(8)	8.6547(8)	13.0004(5)
b (Å)	11.3195(7)		13.499(4)	11.767(2)	9.7979(14)	8.5156(7)	34.528(3)	13.0836(6),
c (Å)	12.3303(7)	15.1096(5)	20.432(7)	13.369(2)	11.6486(19)	17.6367(18)	8.0695(8)	16.1332(7)
α (°)	98.205(3)	90	90	73.246(9)	77.367(8)	97.212(4)	90	103.557(2)
β (°)	115.742(3)	90	98.226(10)	89.373(8)	89.251(8)	100.423(5)	99.643(3)	109.028(2)
γ (°)	110.717(4)	90	90	72.766(8)	88.100(8)	99.725(4)	90	101.021(2)
V (Å^3)	1234.62(15)	2120.08(10)	2145.8(12)	1133.0(3)	814.2(2)	1192.1(2)	2377.4 (4)	2412.61(19)
Z	2	4	4	2	2	2	4	1
Radiation type	Mo $K\alpha$	Mo $K\alpha$	Mo $K\alpha$	Mo $K\alpha$	Mo $K\alpha$	Mo $K\alpha$	Mo $K\alpha$	Mo $K\alpha$
μ (mm^{-1})	0.84	0.97	0.96	0.92	1.25	0.88	0.88	0.66
Crystal size (mm)	0.27×0.23×0.21	0.19×0.12×0.04	0.18×0.17×0.12	0.04×0.17×0.22	0.04×0.09×0.14	0.24×0.22×0.12	0.27×0.22×0.17	0.24×0.22×0.14
Data collection								
Diffractometer	Bruker Kappa Apex2	Bruker Kappa Apex2	Bruker Kappa Apex2	Bruker Kappa Apex2	Bruker Kappa Apex2	Bruker Kappa Apex2	Bruker Kappa Apex2	Bruker Kappa Apex2
Absorption correction	Numerical	Numerical	Numerical	Numerical	Numerical	Numerical	Numerical	Numerical
T_{min}, T_{max}	0.82, 0.84	0.89, 0.96	0.85, 0.89	0.86, 0.96	0.89, 0.95	0.82, 0.90	0.82, 0.86	0.86, 0.91
Reflections								
No. of measured	23,479	10,206	21,484	18,040	14,070	29,881	18,889	25,537
Independent	4,744	1,991	4,500	4,286	3,142	4,610	4,514	9,139
observed [$I > 2.0\sigma(I)$]	3,501	1,601	3,155	3,683	2,396	4,044	3,553	5,996
R_{int}	0.039	0.032	0.015	0.027	0.047	0.020	0.049	0.036
$(\sin\theta/\lambda)_{max}$ (Å^{-1})	0.613	0.611	0.638	0.614	0.616	0.614	0.611	0.615
Refinement								
$R[F^2 > 2\sigma(F^2)]$	0.038	0.025	0.039	0.049	0.041	0.051	0.051	0.065
R_w (F^2)	0.061	0.038	0.060	0.088	0.080	0.102	0.069	0.129
S	1.00	1.00	1.00	1.00	1.00	1.00	1.00	1.00
No. of reflections	3501	1601	3155	3683	2396	4044	3553	5996
No. of parameters	280	124	279	307	232	352	352	596
No. of restraints	0	0	2	0	1	0	0	8
Absolute structure parameter (Flack)	—	0.00(2)	—	—	—	—	—	—
$\Delta\rho_{max}$, $\Delta\rho_{min}$ (e Å^{-3})	0.24, −0.24	0.17, −0.15	0.60, −0.95	0.60, −0.41	0.57, −0.48	0.61, −0.87	0.49, −0.50	0.73, −0.37

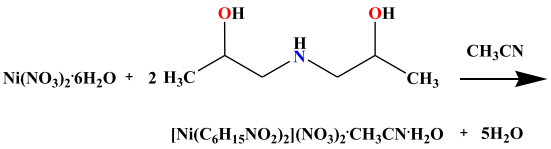

In a slightly modified version of the synthesis of compound **1**, careful handling of the addition of chemical reagents to the reaction mixture led to the surprising isolation of crystalline material $[Ni(C_6H_{15}NO_2)_2](NO_3)_2$ (**2**), which phenomenologically is similar if not identical to **1** (vide infra). The overall stoichiometric reaction leading to **2** is shown below:

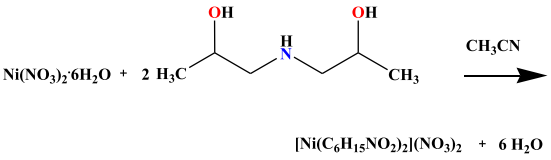

Green crystalline compound $[Ni(C_6H_{15}NO_2)(C_{10}H_8N_2)(NO_3)](NO_3) \bullet 0.25CH_3OH$ (**3**) was synthesized through a reaction between $Ni(NO_3)_2{\cdot}6H_2O$, Imino, and bipy in methanol, using a molar ratio of 1:1:1 at 25 °C. A stoichiometric rendition of the reaction leading to **3** is shown below:

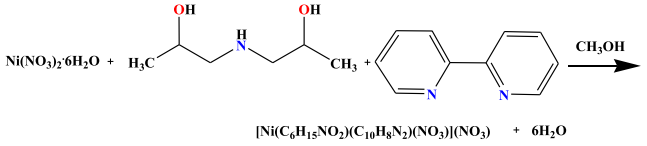

In an analogous reactivity pattern, blue crystalline plates of compound $[Ni(C_6H_{15}NO_2)(C_{12}H_8N_2)(NO_3)](NO_3) \bullet CH_3OH$ (**4**) were isolated through a reaction of $Ni(NO_3)_2{\cdot}6H_2O$ with Imino and phen, in a molar ratio 1:1:1, at 4 °C, in methanol solution. The overall stoichiometric reaction leading to **4** is shown below:

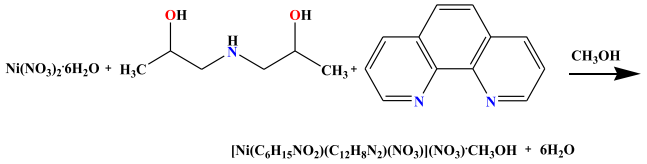

The binary compounds of Ni(II) with an aromatic chelator were synthesized through the same procedure, as stated above, taking into consideration the a) molar ratio, and b) solvent. Specifically, light blue crystalline compound $[Ni(C_{10}H_8N_2)(NO_3)(CH_3CN)(H_2O)_2](NO_3)$ (**5**) was synthesized through a reaction of $Ni(NO_3)_2{\cdot}6H_2O$ and bipy, with a 1:1 molar ratio, at 25 °C, using acetonitrile as a solvent. The overall stoichiometric reaction leading to **5** is shown below:

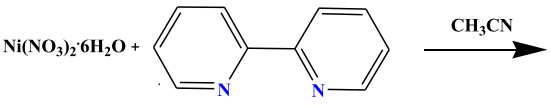

Violet crystalline compound $[Ni(C_{12}H_8N_2)_2(NO_3)(CH_3OH)](NO_3)$ (**6**) was synthesized through a reaction of $Ni(NO_3)_2{\cdot}6H_2O$ and phen, with a 1:2 molar ratio, at 25 °C, in methanol solution. The overall stoichiometric reaction leading to **6** is shown below:

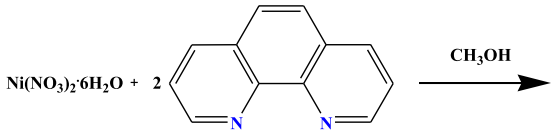

Along the same logic, the reaction between $Ni(NO_3)_2{\cdot}6H_2O$ with phen, in a molar ration 1:3, in the same solvent methanol, led to the isolation of a different material compared to **6**. The reaction below indicates the stoichiometry leading to $[Ni(C_{12}H_8N_2)_2(NO_3)(CH_3OH)](NO_3)$ (**7**).

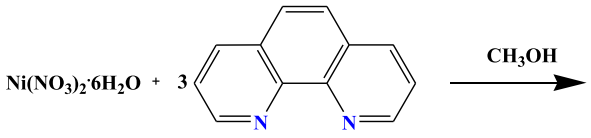

Pink crystalline compound $\{[Ni(C_{12}H_8N_2)_3]_2[Ni(H_2O)_6]\}(NO_3)_6 \bullet 4CH_3CN \bullet H_2O$ (**8**) was synthesized through a reaction of $Ni(NO_3)_2{\cdot}6H_2O$ and phen, with a 1:2 molar ratio, at 4 °C, in acetonitrile solution. The overall stoichiometric reaction leading to **8** is shown below:

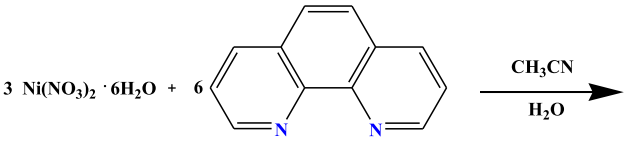

In all cases examined, the employed aromatic chelator binders bipy (**3**,**5**), and phen (**4**,**6**,**7**,**8**) showed that both ligands were crucial for the isolation of crystalline product(s) amenable to further characterization. Methanol was also crucial in achieving a stable crystal structure for the majority of compounds studied.

Essential to the delineation of the structural speciation of the investigated binary and ternary systems of Ni(II) were chemical transformations of emerging species through addition of the employed aromatic chelators (bipy and phen), in line with envisioned structural variants exemplifying the diversity of species. To that end, the stoichiometric chemical transformation of **2** to **3** is shown below:

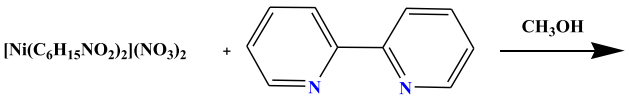

By analogy, the stoichiometric chemical transformation of **2** to **4**, using the aromatic chelator phen in molar ratios **2**:phen of 1:1 and 1:2, is shown below:

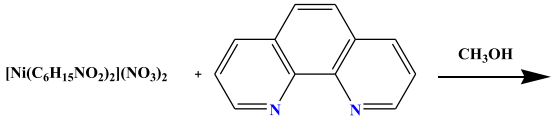

The derived crystalline materials were stable in air for long periods of time. All crystalline materials were soluble in water, methanol (**1**–**8**) and some of them in acetonitrile (**5, 8**).

4.2. Description of X-Ray crystallographic structures

All synthesized compounds exhibit discrete structures. In general, all complexes are mononuclear with distorted octahedral coordination geometry.

Compound **1** crystallizes in the triclinic crystallographic system with space group $P\bar{1}$ and Z = 2 (Table 1). Each asymmetric unit comprises one dicationic $[Ni(iminodipropanol)_2]^{2+}$ complex assembly, two nitrate counter ions, one solvent acetonitrile molecule and one solvent water molecule, all located on general positions. The Imino ligand is fully protonated and coordinated to the Ni(II) center in a tridentate fashion through the two propanol oxygen atoms and the imino nitrogen (Fig. 1A and B). The coordination mode can be best described as forming two five-membered chelate rings, both including the imino nitrogen and the metal ion. In each chelate ring, four of the five atoms (the metal ion, the propanol oxygen, the carbon atom bonded to the previous oxygen and the imino nitrogen) form a mean plane. The two mean planes in both imino ligands can be considered as coplanar forming the final ligand coordination plane. All of the rest of the carbon atoms of the ligand always have the same orientation (above or below the ligand coordination plane). The coordination planes of the two imino ligands are almost perpendicular to each other, forming the final distorted octahedral coordination environment around the central metal ion.

The mean interatomic distances of 2.022 Å for Ni-N and 2.087 Å for Ni-O are typical for complexes with a NiN_2O_4 chromophore. The oxidation state for the metal center Ni(II) was supported through BVS calculations, revealing a value of 1.983. Selected interatomic distances and bond angles are presented in Table 2 and Table 9S.

Hydrogen bonding interactions (Table 1S) between the two of the three nitrate oxygen atoms, the propanol oxygen atoms, the imino nitrogen, and the water oxygen, form a rigid net, keeping all these moieties close together (Fig. 1SA and B). Each water oxygen is involved in three interactions in a Y type mode, with one propanolic and two nitrate oxygen atoms from different anions. Each of the two nitrate oxygen atoms is bridging either a propanol oxygen and an imino nitrogen or a water oxygen and an imino nitrogen. All interactions expand in three dimensions and ultimately lead to a final 3D crystal lattice (Fig. 1C).

Complex **2** crystallizes in the tetragonal crystallographic system with space group $P\bar{4}2_1c$ and Z = 4. Each asymmetric unit comprises one dicationic $[Ni(iminodipropanol)_2]^{2+}$ complex assembly and two nitrate counter ions (Fig. 2A and B). The Ni(II) ion is located on a special position. The imino ligand is fully protonated and coordinated to the Ni(II) center in a tridentate fashion through the two propanol oxygen atoms and the imino nitrogen. The coordination mode can be described as one involving two five-membered chelate rings, with one common edge forming from the imino nitrogen and the metal ion. These two chelate rings are significantly distorted from planarity and their mean planes are nearly perpendicular. The Imino ligand upon coordination can be considered as 90° folded around the Ni-N bond axis to occupy half the octahedral coordination sphere around the metal ion. The three remaining coordination atoms are coming from a symmetry-generated Imino ligand with respect to the 4-fold rotoinversion axis passing through Ni(II). BVS theoretical calculations of the metal center oxidation state reveal a value of 1.956.

The mean interatomic distances of 2.050 Å for Ni-N and 2.062 Å for Ni-O are typical for complexes with a NiN_2O_4 chromophore. Selected

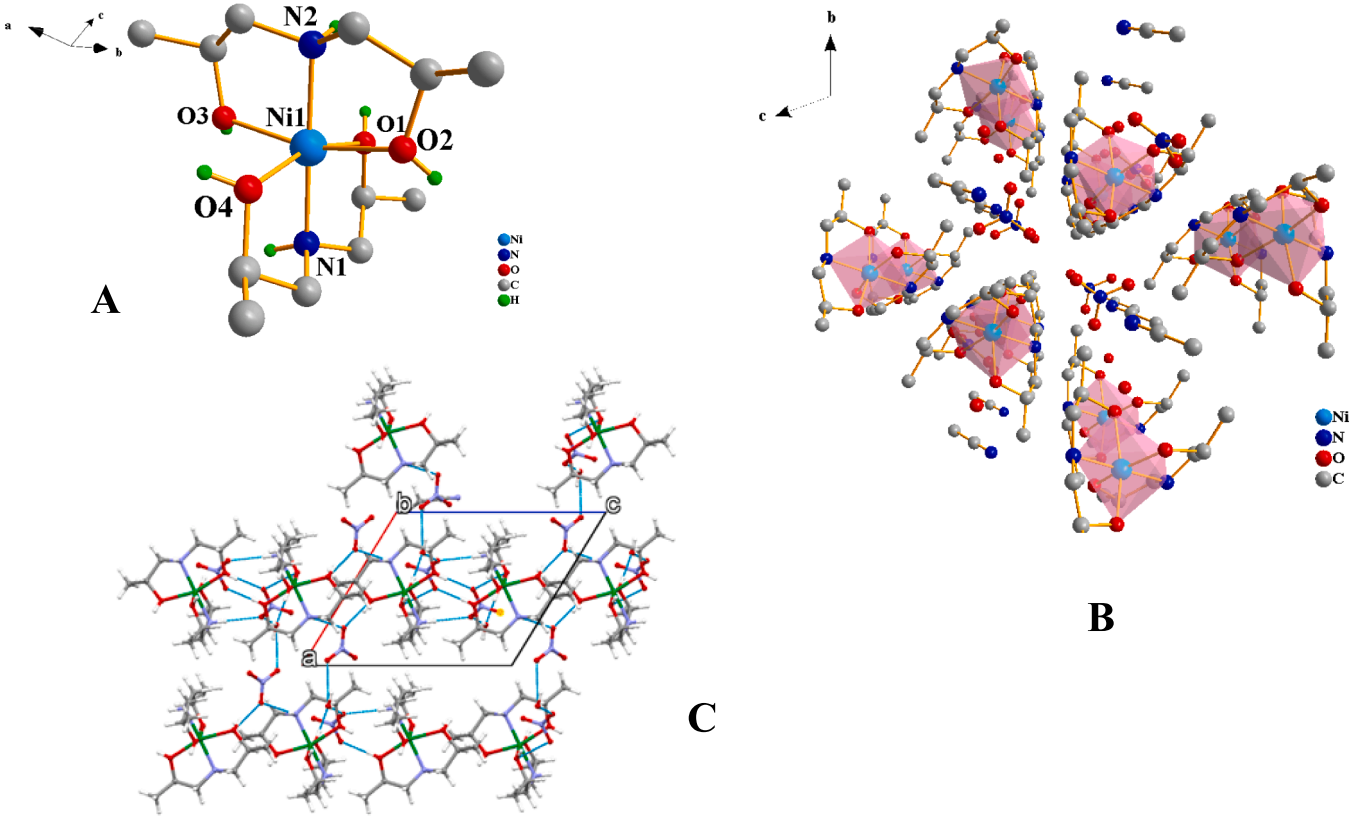

Fig. 1. A. Diamond plot of complex cationic assembly $[Ni(C_6H_{15}NO_2)_2]^{2+}$ in **1**. **B.** Structure of **1** along the *a* crystallographic axis. **C.** Hydrogen bonding interactions (blue dashed lines) in **1**. View along the *b* axis. ((Colour online.))

Table 2
Summary of crystallographic data on compounds $[Ni(C_6H_{15}NO_2)_2](NO_3)_2 \bullet CH_3CN \bullet H_2O$ (**1**), $[Ni(C_6H_{15}NO_2)_2](NO_3)_2$ (**2**), $[Ni(C_6H_{15}NO_2)(C_{10}H_8N_2)(NO_3)](NO_3) \bullet 0.25CH_3OH$ (**3**), $[Ni(C_6H_{15}NO_2)(C_{12}H_8N_2)(NO_3)](NO_3) \bullet CH_3OH$ (**4**), $[Ni(C_{10}H_8N_2)(NO_3)(CH_3CN)(H_2O)_2](NO_3)$ (**5**), $[Ni(C_{12}H_8N_2)_2(NO_3)(CH_3OH)](NO_3)$ (**6**), $[Ni(C_{12}H_8N_2)_2(NO_3)(CH_3OH)](NO_3)$ (**7**), $\{[Ni(C_{12}H_8N_2)_3]_2[Ni(H_2O)_6]\}(NO_3)_6 \bullet 4CH_3CN \bullet H_2O$ (**8**).

Bond Distances (Å)

1		**2**		**3**		**4**	
Ni(1)—O(1)	2.070(2)	Ni(1)—O(1)	2.061(2)	Ni(1)—N(1)	2.068(2)	Ni(1)—O(1)	2.096(2)
Ni(1)—O(2)	2.101(2)	Ni(1)—O(2)	2.084(2)	Ni(1)—N(2)	2.059(3)	Ni(1)—O(2)	2.109(2)
Ni(1)—O(3)	2.095(2)	Ni(1)—N(1)	2.050(2)	Ni(1)—O(1)	2.104(2)	Ni(1)—N(1)	2.071(3)
Ni(1)—O(4)	2.081(2)	N(2)—O(3)	1.237(3)	Ni(1)—O(2)	2.092(2)	Ni(1)—N(2)	2.054(3)
Ni(1)—N(1)	2.022(2)	N(2)—O(5)	1.222(3)	Ni(1)—O(3)	2.069(2)	Ni(1)—N(3)	2.066(3)
5		**6**		**7**		**8**	
Ni(1)—O(1)	2.076(3)	Ni(1)—N(2)	2.066(4)	Ni(1)—N(1)	2.075(3)	Ni(1)—N(1)	2.083(4)
Ni(1)—O(2)	2.083(2)	Ni(1)—N(3)	2.070(3)	Ni(1)—N(3)	2.091(3)	Ni(1)—N(2)	2.102(4)
Ni(1)—O(3)	2.099(3)	Ni(1)—N(4)	2.085(3)	Ni(1)—N(4)	2.073(3)	Ni(2)—O(1)	2.049(3)
Ni(1)—N(1)	2.062 (3)	Ni(1)—O(1)	2.111(3)	Ni(1)—O(1)	2.100(2)	Ni(2)—O(2)	2.033(4)
Ni(1)—N(2)	2.058 (3)	Ni(1)—O(2)	2.093(3)			Ni(2)—O(3)	2.042(4)

Angles (°)

1		**2**		**3**		**4**	
N(1)—Ni(1)—N(2)	179.15(10)	O(1)—Ni(1)—O(2)	93.14(7)	N(1)—Ni(1)—N(2)	95.77(11)	N(1)—Ni(1)—N(2)	94.03(10)
N(1)—Ni(1)—O(1)	81.63(8)	O(1)—Ni(1)—N(1)	82.57(7)	N(1)—Ni(1)—N(3)	97.07(11)	N(1)—Ni(1)—N(3)	95.98(11)
N(2)—Ni(1)—O(1)	97.77(8)	$O(2)^{i}$—Ni(1)—O(1)	89.36(7)	N(2)—Ni(1)—N(3)	79.33(10)	N(2)—Ni(1)—N(3)	81.08(10)
N(2)—Ni(1)—O(2)	80.94(9)	$N(1)^{i}$—Ni(1)—O(1)	168.92(8)	N(2)—Ni(1)—O(1)	93.73(10)	N(2)—Ni(1)—O(1)	172.59(9)
O(1)—Ni(1)—O(2)	89.98(8)	$O(2)^{i}$—Ni(1)—O(2)	176.41(10)	N(3)—Ni(1)—O(1)	172.56(10)	N(3)—Ni(1)—O(1)	93.69(10)
N(1)—Ni(1)—O(3)	99.03(9)	$N(1)^{i}$—Ni(1)—O(2)	96.22(8)	N(2)—Ni(1)—O(2)	172.59(9)	N(1)—Ni(1)—O(2)	81.68(10)
O(1)—Ni(1)—O(3)	97.62(8)	$N(1)^{i}$—Ni(1)—N(1)	104.63(12)	N(3)—Ni(1)—O(2)	94.56(10)	N(3)—Ni(1)—O(2)	173.57(10)
O(2)—Ni(1)—O(3)	161.77(7)	O(4)—N(2)—O(5)	118.5(2)	O(1)—Ni(1)—O(2)	92.15(9)	O(1)—Ni(1)—O(2)	91.88(10)
N(2)—Ni(1)—O(4)	99.12(8)			N(1)—Ni(1)—O(3)	173.99(9)	N(1)—Ni(1)—O(3)	175.50(11)
O(1)—Ni(1)—O(4)	161.91(7)			N(2)—Ni(1)—O(3)	87.11(9)		
		(i) $-x, -y+1, z$					
5		**6**		**7**		**8**	
N(1)—Ni(1)—N(2)	79.75(12)	N(1)—Ni(1)—N(2)	81.03(15)	N(1)—Ni(1)—N(2)	80.46(11)	N(1)—Ni(1)—N(2)	79.55(17)
N(1)—Ni(1)—N(3)	93.51(12)	N(1)—Ni(1)—N(3)	98.13(12)	N(1)—Ni(1)—N(3)	95.66(11)	N(1)—Ni(1)—N(3)	95.44(15)
N(2)—Ni(1)—N(3)	172.79(12)	N(1)—Ni(1)—N(4)	177.63(14)	N(2)—Ni(1)—N(3)	175.79(11)	N(2)—Ni(1)—N(3)	173.01(16)
N(1)—Ni(1)—O(1)	89.78(11)	N(3)—Ni(1)—N(4)	80.19(12)	N(1)—Ni(1)—O(1)	89.41(10)	N(1)—Ni(1)—N(4)	93.36(15)
N(1)—Ni(1)—O(2)	177.93(12)	N(3)—Ni(1)—O(1)	171.89(14)	N(3)—Ni(1)—O(1)	94.66(10)	O(1)—Ni(2)—O(3)	88.10(15)
N(2)—Ni(1)—O(2)	99.56(11)	N(1)—Ni(1)—O(2)	95.26(14)	N(4)—Ni(1)—O(1)	172.28(11)	$O(1)^{i}$—Ni(2)—O(1)	179.994
O(1)—Ni(1)—O(2)	88.25(10)	N(2)—Ni(1)—O(2)	174.50(13)	N(2)—Ni(1)—O(2)	97.42(11)	$O(2)^{i}$—Ni(2)—O(1)	92.50(15)
O(2)—Ni(1)—O(3)	92.41(10)	O(1)—Ni(1)—O(2)	84.84(13)	O(1)—Ni(1)—O(2)	85.26(10)	$O(3)^{i}$—Ni(2)—O(2)	88.13(17)
						(i) $-x+2, -y+1, -z+2$	

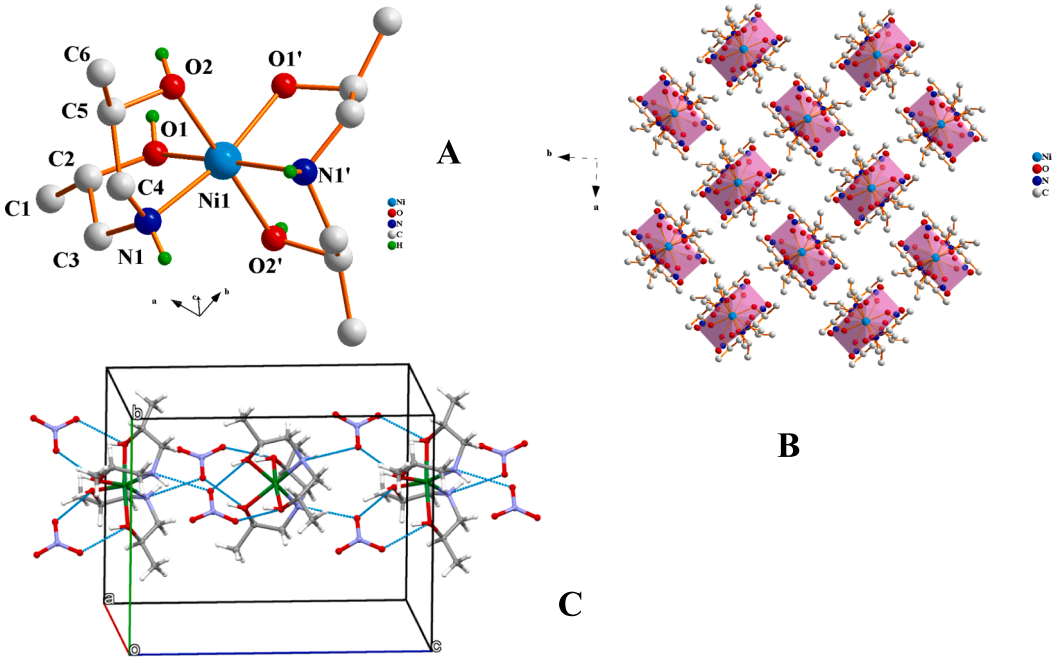

Fig. 2. A. Diamond plot of complex cationic assembly $[Ni(C_6H_{15}NO_2)_2]^{2+}$ in **2**. **B.** Structure of **2** along the *c* crystallographic axis. **C.** Hydrogen bonding interactions (blue dashed lines) in **2**. ((Colour online.))

interatomic distances and bond angles are presented in Table 2 and Table 9S.

Hydrogen bonding interactions arise mainly between the two of the three nitrate oxygen atoms O(3) and O(5) and both propanolic oxygen atoms as well as the imino nitrogen from the parent and neighboring complexes. All of the previous interactions form a rigid net, keeping all atoms involved close together. Atom O(3) acts as a bridging agent between neighboring groups. These interactions (Table 2S) form infinite chains parallel to the *c* crystallographic axis and lead to a final 1D crystal lattice (Fig. 2C).

Complex **3** crystallizes in the monoclinic crystallographic system with space group $P2_1/n$ and Z = 4 (Fig. 3A). Each asymmetric unit comprises one monocationic $[Ni(iminodipropanol)(bipy)(NO_3)]^+$ complex assembly, one nitrate counter ion, and a quarter of a solvent methanol molecule - all placed on general positions. The Imino ligand is fully protonated and coordinated to the Ni(II) cation in a tridentate fashion, through the two propanol oxygen atoms and the imino nitrogen. The ligand can be considered, as in the case of complex **2**, as ~ 90° folded around the Ni-N bond axis, occupying three of the totally six positions of the octahedral coordination sphere around the metal ion. Two more positions are occupied by the nitrogen atoms of the chelate bipy ligand. The sixth position is occupied by an oxygen atom of a coordinated nitrato anion.

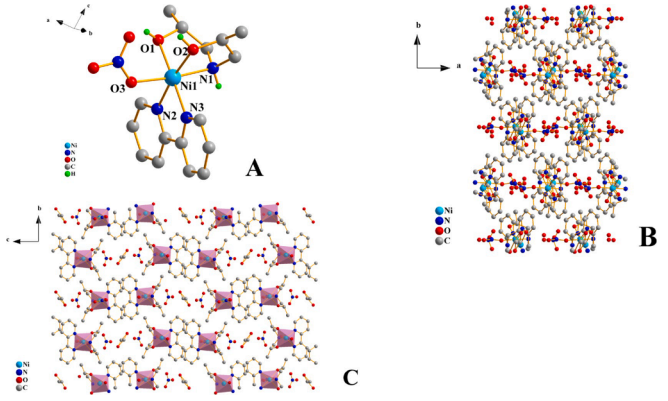

Fig. 3. A. Diamond plot of complex cationic assembly $[Ni(C_6H_{15}NO_2)(C_{10}H_8N_2)(NO_3)]^+$ in **3**. **B.** Structure of **3** along the *c* crystallographic axis. **C.** Structure of **3** along the *α* crystallographic axis.

The mean interatomic distances of 2.065 Å for Ni-N and 2.089 Å for Ni-O are typical for complexes with a NiN_3O_3 chromophore. The oxidation state of Ni(II) was supported through BVS calculations, revealing a value of 1.914. Selected interatomic distances and bond angles are presented in Table 2 and Table 9S.

Hydrogen bonding interactions (Table 3S), forming between the nitrate and propanolic oxygen atoms, keep these atoms close together. The oxygen atom of the severely disordered solvent methanol is also interacting with the free nitrate anion (Fig. 3B and C). All of the aforementioned interactions are local and consequently do not form an expanded crystal lattice.

Complex **4** crystallizes in the triclinic crystallographic system with space group $P\bar{1}$ and Z = 2 (Fig. 4A). Each asymmetric unit comprises one monocationic $[Ni(iminodipropanol)(phen)(NO_3)]^+$ complex assembly, one nitrate counter ion and one solvent methanol molecule, with all atoms occupying general positions. Complex **4** differs from **3** in that it contains phen instead of bipy. The Imino ligand is again fully protonated and coordinated to the Ni(II) cation in a bis-chelate tridentate fashion, adopting again the 90° folded configuration previously described. The three remaining coordination positions are occupied by the nitrogen atoms of the chelate phenanthroline ligand and an oxygen atom from a singly coordinated nitrato anion. The theoretical Ni(II) oxidation state, calculated through BVS, is 1.931.

The mean interatomic distances of 2.063 Å for Ni-N and 2.085 Å for Ni-O are typical for complexes with a NiN_3O_3 chromophore. Selected interatomic distances, bond angles, and hydrogen interactions are presented in Table 2 and Table 9S and Table 4S, respectively.

The oxygen atoms of the free nitrate anion and one non-coordinated oxygen atom from the coordinated nitrato anion are engaged in hydrogen bonding interactions with the propanol oxygen atoms and the solvent methanol molecule. All of these interactions are local, creating a non-expanded crystal lattice, yet one keeping the asymmetric unit

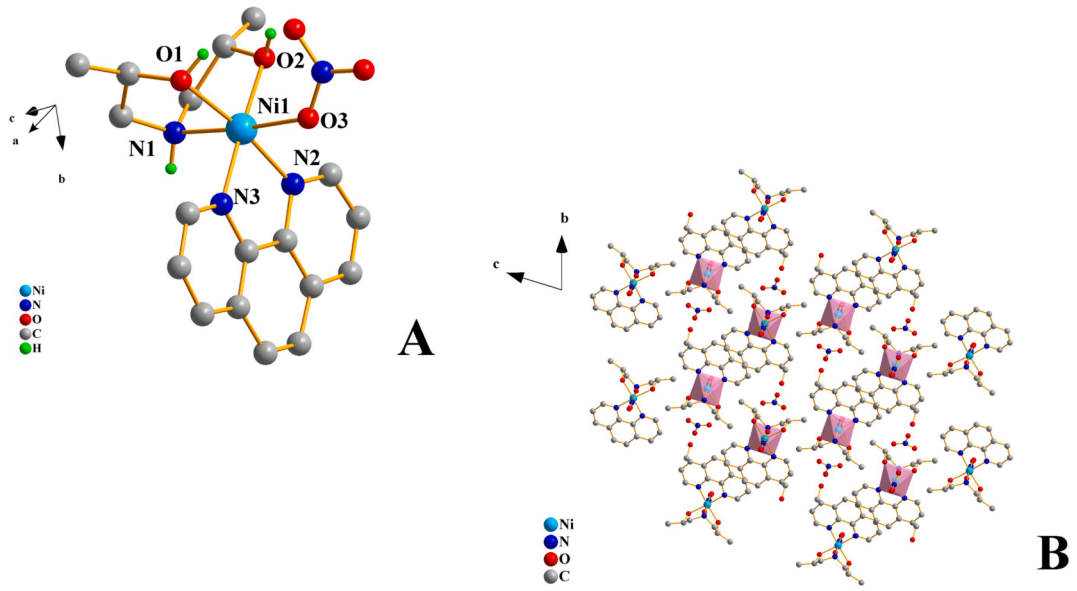

Fig. 4. A. Diamond plot of complex cationic assembly $[Ni(C_6H_{15}NO_2)(C_{12}H_8N_2)(NO_3)]^+$ in **4**. **B.** Structure of **4** along the *α* crystallographic axis.

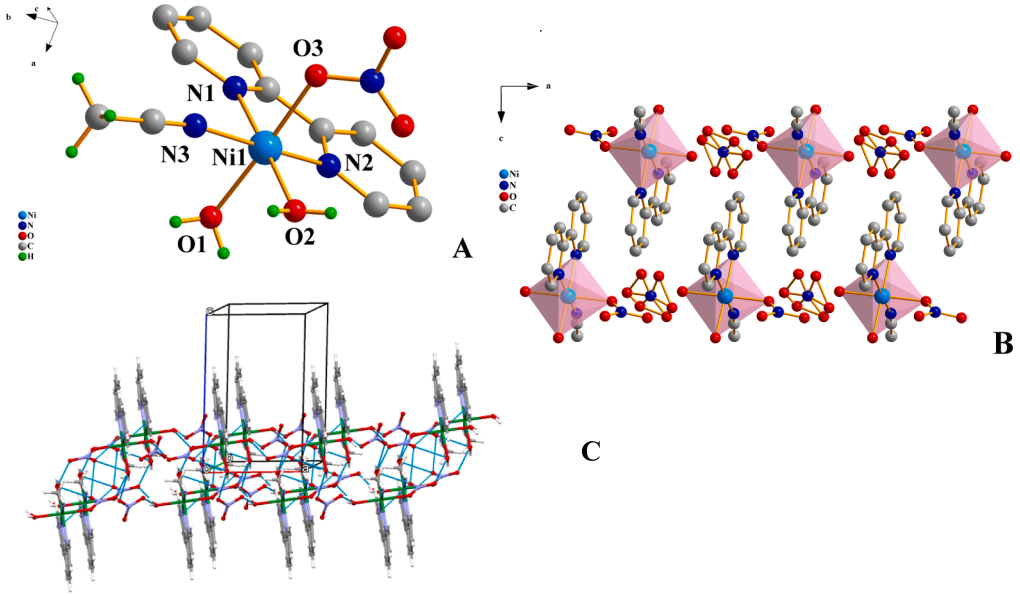

Fig. 5. A. Diamond plot of complex cationic assembly $[Ni(C_{10}H_8N_2)(NO_3)(CH_3CN)(H_2O)_2]^+$ in **5**. **B.** Structure of **5** along the *b* crystallographic axis. **C.** Hydrogen bonding interactions (blue dashed lines) in **5.** ((Colour online.))

contents close together (Fig. 4B).

Complex **5** crystallizes in the triclinic crystallographic system with space group $P\bar{1}$ and Z = 2 (Fig. 5A). Each asymmetric unit comprises one singly cationic $[Ni(bipy)(NO_3)(CH_3CN)(H_2O)_2]^+$ complex assembly and one nitrate counter ion, with oxygen atoms disordered over two equivalent positions. The bipy ligand is coordinated in a usual chelate bidentate fashion to the metal ion through both the nitrogen atoms (Fig. 5B). Three coordination sites are occupied by oxygen atoms coming from one singly coordinated nitrato anion and two water molecules. The sixth site of the distorted octahedral coordination polyhedron is occupied by a nitrogen atom of an acetonitrile ligand.

The mean interatomic distances of 2.060 Å for Ni-N and 2.086 Å for Ni-O are typical for complexes with a NiN_3O_3 chromophore. The oxidation state assignment for the nickel center was supported through BVS calculations, revealing a value of 1.934. Selected interatomic distances and bond angles are presented in Table 2 and Table 9S.

The disordered oxygen atoms of the free nitrate anion and the non-coordinated oxygen atoms from the coordinated nitrato anion as well as the water ligands form a complex hydrogen bonding interaction net (Table 5S). All of these interactions expand in space, creating planes parallel to *a*0*b* crystallographic plane and a final 2D crystal lattice, keeping these crystal components close together (Fig. 5C).

Compounds **6** and **7** have the same total and moiety molecular formula. Compound **6** crystallizes in the triclinic crystallographic system with space group $P\bar{1}$ and Z = 2 (Fig. 6A and B), with compound **7** crystallizing in the monoclinic crystallographic system with space group $P2_1/c$ and Z = 4 (Fig. 7A and B). Both compound asymmetric units emerge from a mononuclear monocationic $[Ni(phen)_2(NO_3)(CH_3OH)]^+$ complex assembly together with a nitrate counter anion. Both phen ligands in both complexes are coordinated in a chelate bidentate mode

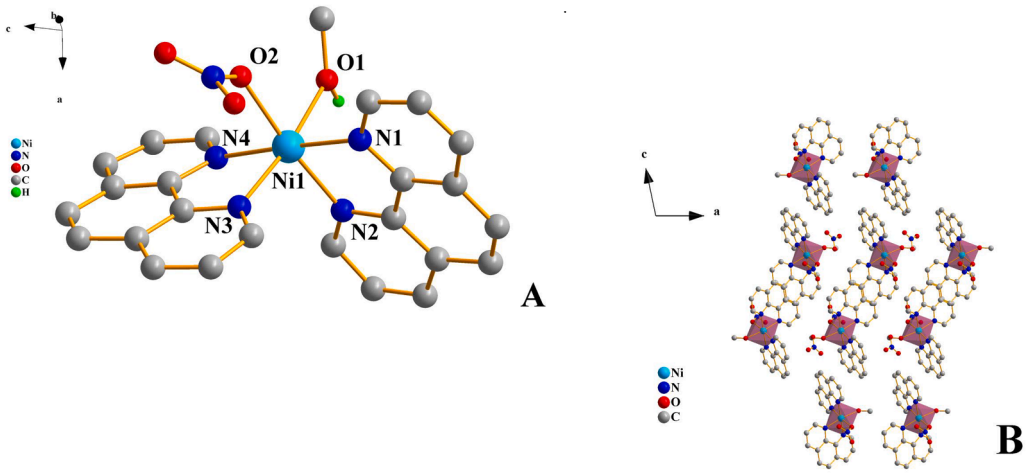

Fig. 6. A. Diamond plot of complex cationic assembly $[Ni(C_{12}H_8N_2)_2(NO_3)(CH_3OH)]^+$ in **6**. **B.** Structure of **6** along the *b* crystallographic axis.

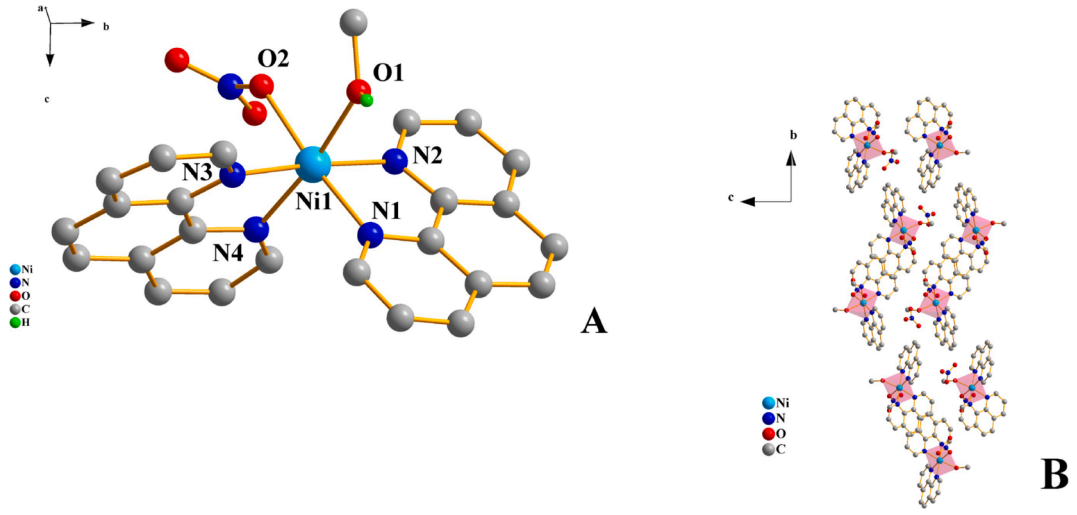

Fig. 7. A. Diamond plot of complex cationic assembly $[Ni(C_{12}H_8N_2)_2(NO_3)(CH_3OH)]^+$ in **7**. **B.** Structure of **7** along the *α* crystallographic axis.

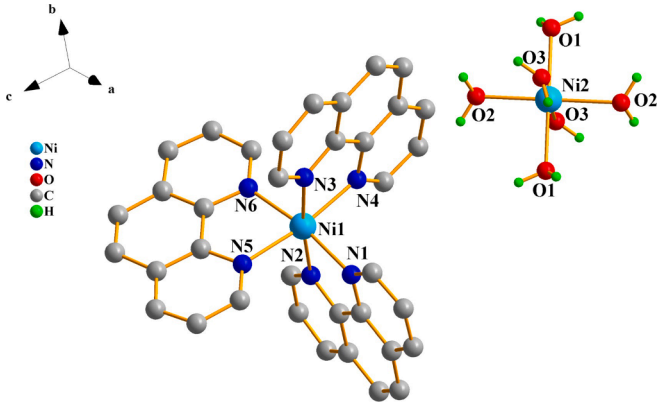

Fig. 8. Diamond plot of complex cationic assemblies $[Ni(C_{12}H_8N_2)_3]^{2+}$ and $[Ni(H_2O)_6]^{2+}$ in **8**.

through the nitrogen atoms, with each phen nitrogen occupying one axial and one equatorial position of the octahedral coordination sphere around the Ni(II) ion center. The coordinated oxygen atoms from the monodentate nitrato ligand and the ligand methanol molecule in both complexes are occupying *cis* equatorial positions of the distorted octahedron. In view of all of these features, the solid-state complexes are structurally distinct, exemplifying the phenomenon of polymorphism.

The mean interatomic distances in the title complexes are 2.071 Å for Ni-N and 2.103 Å for Ni-O. The corresponding distances in complex **7** are 2.079 Å and 2.100 Å, very close to those of complex **6**. All coordination bond distances are typical for complexes with a NiN_4O_2 chromophore. Selected interatomic distances and bond angles are presented in Table 2 and Table 9S. In both cases, the oxidation state of the nickel center was revealed through theoretical calculations via BVS, delivering values of 1.891 for **6** and 1.870 for **7**.

Hydrogen bonding interactions (Table 6S and 7S) in both complexes are localized only between the oxygen atom of the methanol ligand and the free nitrate anion in the same asymmetric unit. The only difference is that in complex **6**, the methanolic hydrogen atom interacts with one of the free nitrate ion oxygen atoms instead of two oxygen atoms in the case of complex **7**.

Compound **8** crystallizes in the triclinic crystallographic system with space group $P\bar{1}$ and Z = 1 (Fig. 8). The unit cell comprises two mononuclear dicationic $[Ni(phen)_3]^{2+}$ complex assemblies, one hexaaquanickel(II) dicationic $[Ni(H_2O)_6]^{2+}$ complex, six nitrate anions,

four severely disordered solvent acetonitrile molecules and one disordered solvent water molecule. All three phenanthroline ligands in the $[Ni(phen)_3]^{2+}$ complex are coordinated in a typical chelate bidentate mode through the nitrogen atoms, giving rise to a disordered octahedral coordination environment around the nickel center. The interatomic distances for Ni-N are in the range 2.082–2.102 Å and the bite angles are in the range 79.55–80.10°, being typical for complexes with a NiN_6 chromophore bearing phenanthroline ligands. Selected interatomic distances and bond angles are presented in Table 2 and Table 9S. The hexaaquanickel(II) $[Ni(H_2O)_6]^{2+}$ complex presents a nearly normal octahedral coordination, with mean Ni-O distances of 2.041 Å and angles in the range of 87.50(15) to 92.50(15) and/or 180° (due to symmetry reasons). The oxidation state of the Ni(II) metal center, derived through BVS calculations, was 1.863.

Hydrogen bonding interactions (Table 8S) between all water ligands of the complex $[Ni(H_2O)_6]^{2+}$ as well as the solvent water and the nitrate anions can be found in the crystal structure of **8**. All of these interactions emerged between components of the same cell and can be characterized as local, not giving rise to a special lattice dimensionality.

4.3. Hirshfeld and electrostatic potential surface analysis

Hirshfeld and electrostatic potential surface analysis were carried out on structures **1**–**8** and the 2D Fingerprint plots were used to describe and quantify the appropriate intermolecular interactions. To that end, surface analysis of compounds **1**–**2** (Fig. 2SA and B) was pursued over d_{norm} mapping, with the most intense interactions emanating via the Imino ligand and water molecule or nitrate anion in the crystal structure, shown through red spots. Deep red spots are localized on the O-terminal alcoholic oxygen atoms of the Imino ligand, depicting the O—H···O interactions (Fig. 2S**C**). Some more visible red spots of smaller size correspond to C—H···O or N—H···O or H···H and weaker or long range interactions. Compared to the surface of compound **2**, the red spots are localized only on O-terminal groups, as shown in the front view of **2** (Fig. 2S**D**), with the weaker ones on the *N*-terminal groups (Fig. 2S**E**) exemplifying N—H···O or H···H interactions. The electrostatic potential of **1** (Fig. 3S**A**) projects a donor-based assembly (blue surface on Fig. 3S**B**), including small red areas around the acceptor O-terminal alcoholic groups of the Imino ligand. Due to the fact that no solvent molecule exists in the crystal structure of compound **2** (Fig. 3S**C**), in the vicinity of the complex assembly, there is more negative electrostatic potential (highlighted red bulky surfaces) close to the OH groups of the Imino ligand (Fig. 3S**D**), thereby depicting incorporation of O-terminal groups in more intense O—H···O interactions compared to that of compound **1**. The collective behavior is in agreement with the interactions pointed out in 2D Fingerprint plots, as a proportion of the overall activity of each compound shown comparatively in Fig. 4S.

The comparative results of surface analysis, electrostatic potential, and 2D Fingerprint plots for the ternary systems in compounds **3** and **4**, reflect significant interactions between a) the OH groups of the bound Imino ligand and nitrato anion, and b) the OH groups of the bound Imino ligand and the nitrate counter ion in the lattice architecture, encompassing O—H···O and H···H interactions. The aforementioned interactions from the internal surface of the selected molecules (Fig. 9A

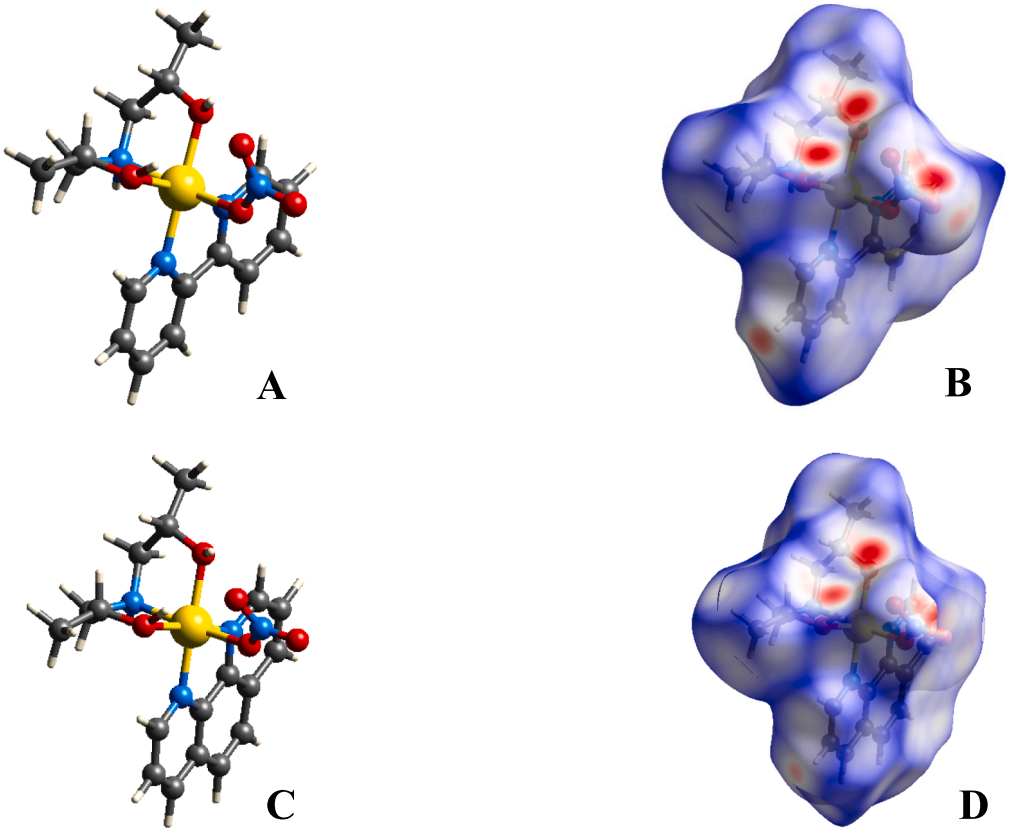

Fig. 9. A. Crystal Explorer plot of **3**. **B.** d_{norm} mapping of **3**. **C.** Crystal Explorer plot of **4**. **D.** d_{norm} mapping of **4**.

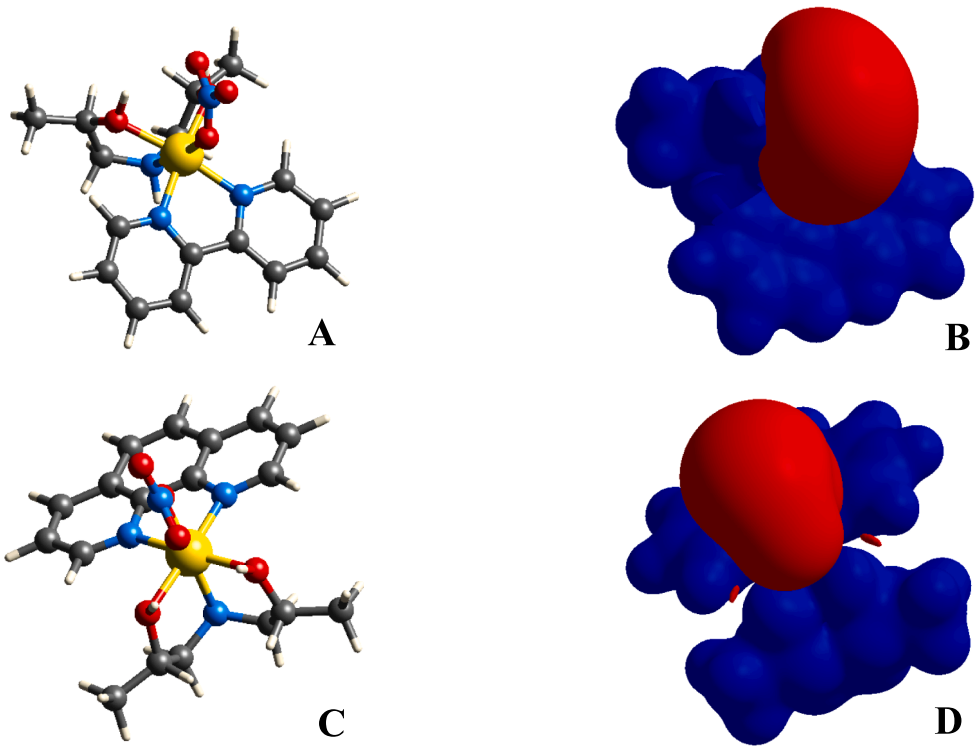

Fig. 10. A. Crystal Explorer plot of **3**. **B.** Electrostatic potential surface of **3**. **C.** Crystal Explorer plot of **4**. **D.** Electrostatic potential surface of **4**.

and C) are well-established and confirmed through the red spots on the d_{norm} mapped surface (Fig. 9B and D**)**. The d_{norm} mapping reveals also blue and white regions as well as red highlighted spots, relevant to (showing the interactions close to or larger than Van der Walls contacts) H···C/C···H interactions of the benzene rings of the phen and bipy chelators in neighboring molecules. The overall surface of compounds **3** and **4 (**Fig. 10A and C**)**, involving the metal center, the Imino ligand, and the aromatic chelator, is projected as donor area, highlighted with a blue color in the electrostatic potential analysis. The nitrato anion is correspondingly projected as an acceptor target group, with negative electrostatic potential, highlighted with a red surface. Compound **4**, shows interesting negative charge distributions around the O-terminal alcoholic groups of the Imino ligand, thus reflecting more negative electrostatic potential on the molecular surface as shown comparatively to compound **3,** in Fig. 10B and D. The collective distinct interactions in compounds **3** and **4** are shown with sharp spikes in Fig. 11, with a pattern of diffuse points between spikes in H···H interactions emanating from cyclic hydrogen bonding. As a result, the specific integrations reveal higher contributions (46.6%) to the overall behavior of compound **3** compared to compound **4** (43.9%).

The intermolecular interactions of the binary system in compound **5** (Fig. 5SA), containing the chelator bipy, were investigated over d_{norm}, d_i, and d_e. The emerging interactions are visible though broad deep red (d_{norm}) or bright orange spots (d_i and d_e) in surface mapping. The bound water molecules and the nitrato anion are the main target groups incorporated in intermolecular interactions depicted with deep red spots on d_{norm} surfaces (Fig. 5S**B**). Specifically, the bound water molecules are responsible for internal interactions, reflected through deep red and bright orange spots in d_i (Fig. 5S**C**) and d_e (Fig. 5S**D**) mapped surfaces, respectively. The bound nitrato anion exhibits the reverse activity, as shown in Fig. 5S**C and D**. The aforementioned groups (Fig. 6S**A**) bound into the molecular assembly are exemplified through negative electrostatic potential distributions, whereas the entire molecule is a donor-based assembly (Fig. 6S**B**). Typical intermolecular H···H, O—H···O, and N—H and C—C interactions are also well-defined by 2D Fingerprint plots. The deconvoluted plots emphasize the distinct contribution of the interactions, as shown in the plots of Fig. 6S**C**.

In the case of the binary systems in compounds **6** (Fig. 7S**A**) and **7** (Fig. 7S**C**), both containing phen, d_{norm} mapping shows the most significant interactions corresponding to O—H···O and C—H···O hydrogen bonds, involving the a) nickel-bound methanol moiety and the nitrate counter anion in the lattice, and b) C—H bonds of the bound aromatic chelator in the Ni(II)-complex and the bound nitrato anion in the abutting Ni(II)-complex assembly. The observed interactions are shown with deep red spots on the surface of the molecule, as illustrated in Fig. 7S**B and D**. The white areas correspond to distances close to Van der Waals contacts, thus indicating the presence of H···H interactions, with the blue patches revealing distant regions from the neighboring molecules involving no interactions. In complement to the aforementioned observations, the charge distribution, shown in Fig. 8S**B** for compound **6** (Fig. 8S**A**) and Fig. 8S**D** for compound **7** (Fig. 8S**C**), indicates that the bound nitrato anion and alcoholic group act as donors and the two phen chelators act as acceptors, collectively exemplified through the blue (positive) and red (negative electrostatic potentials) surfaces shown, respectively. The above noted interactions are confirmed through analysis of the H···H, O—H···O, and C···H contributions, using the deconvoluted 2D Fingerprint plots for **6** and **7**, as shown comparatively in Fig. 9S. The highest contribution is that from H-bond interactions, emerging as distinct spikes on the plots, with a proportion of ~ 32%. A pair of wings depict the typical C—H···C interactions, rising up to 24.4%

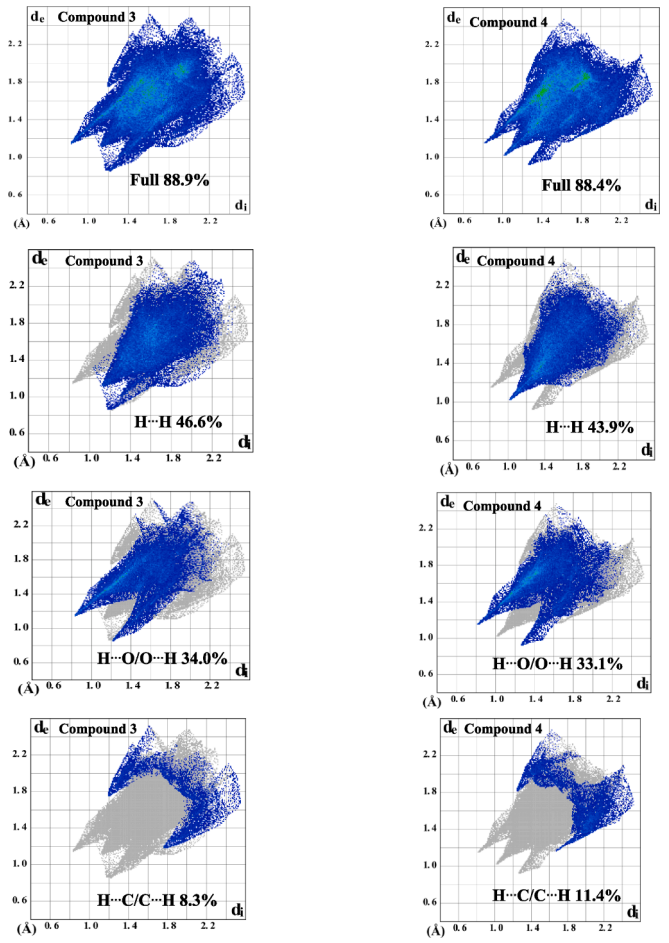

Fig. 11. Full 2D Fingerprint and deconvoluted plots of significant interactions of compounds **3** (left) and **4** (right), along with relevant contributions.

for **6** and 25.8% for **7**. Other contacts were also pointed out through the deconvoluted fingerprint plots, involving N···H (~3.0%) and C···C (~7.0%) interactions.

In the case of compound **8** (Fig. 10S**A**), d_{norm} mapping shows deep red spots on the C—H groups of the phen chelator (Fig. 10S**B**), thus indicating a) C—H···O interactions between the bound phen molecule and the lattice nitrate counter anion, and/or b) C—H···N interactions between the bound phen molecule and the lattice acetonitrile solvent. The three bound phen chelators of the molecular assembly (Fig. 10S**C**) are collectively bathed in red areas, whereas the entire molecule involving the aromatic rings is blue, thus indicating negative and positive electrostatic potential distributions (Fig. 10S**D**), respectively. The C—H···C interactions are depicted with two pairs of wings in the deconvoluted 2D Fingerprint plots, with their contribution standing at 20.0%, as shown in the plots of Fig. 10S**E**.

4.4. Electronic structure modeling

DFT calculations were performed to investigate the energetics of one complex assembly in comparison to the other (vide infra). Providing a direct comparison of the total energy between complex assemblies in solution does not provide useful information, because each unit cell contains different numbers and types of atoms. The normalized formation energy was calculated instead, as the total energy of the system in solution minus the total energy of its constituent atoms, over the number of atoms (Fig. 12). It is observed that it's easier to form complex **1** than **2** by 33 meV per atom. The normalized formation energy difference, ΔE, between complex **2** and **3** is 450 meV per atom, and between **3** and **4** is 65 meV per atom, which explains why transformation from **2** to **3** and **4** proceeds uneventfully; it would take a large amount of energy to reverse the process from **3** to **2**. However, transformation of complex **4** to **6** and **7** does not proceed, thereby indicating a large energy activation barrier between them, although ΔE between **4** and **6** is 551 meV per atom, and between **6** and **7** is 43 meV.

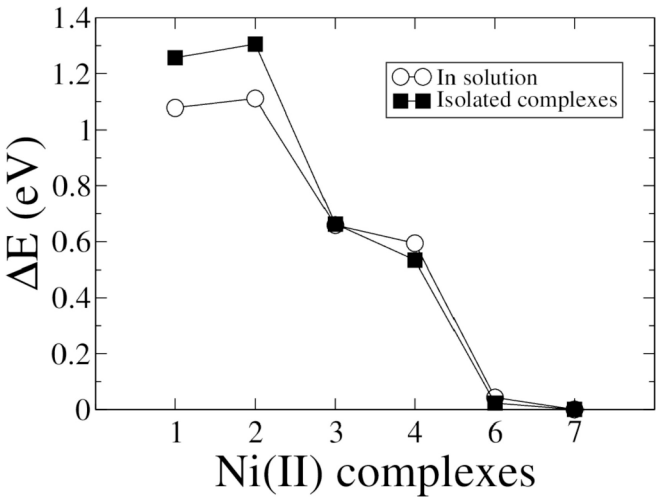

Fig. 12. Normalized formation energy difference between Ni(II) complexes **1**, **2**, **3**, **4**, **6**, and **7**. All calculations were performed at fixed geometry in solution, for all unit cells (circles) and the isolated complexes at their geometry in solution (squares). All energy differences are per atom.

4.5. FT-IR spectroscopy

The FT-IR spectra of compounds **1**–**8** in KBr exhibit shifted bands related to ν(C—N) bond vibrations in bipy and phen, thus indicating bond formation to metal ions. Specifically, strong ν(C—N) bond vibrations of bipy [36] emerge at 1599 cm^{-1} for **3**, and 1602 cm^{-1} for **5**. In compound **4**, strong ν(C—N) vibrations are shifted to 1387 cm^{-1} (broad feature) and in compounds **6**, **7**, and **8** strong ν(C—N) bond vibrations are observed at 1429 cm^{-1}, compared to free phen (1419 cm^{-1}) [37]. Furthermore, bands in the range from a) 3167 to 2870 cm^{-1} for **1** and **2**, b) 3263 to 2934 cm^{-1} for **3**, and c) 3218 to 2768 cm^{-1} for **4**, reveal the presence of the imino chelate ligand OH groups bound to the metal center. An intense and broad absorption band in the range 3030–3650 cm^{-1} for **5**, and 3060–3560 cm^{-1} for **8** corresponds to coordinated water molecules [38]. In the case of **1** and **2** congener complexes, infrared spectral fingerprints are difficult to differentiate from one another, with ostensible features in **1** consistently emerging as two discrete peaks at 1210 and 1109 cm^{-1}, which do not appear in **2**.

Frequencies in the range 415–490 cm^{-1} for compounds **1**–**8** suggest the presence of both chelator ligands and Ni-N bond vibrations, thus indicating changes in the vibrational pattern of the ligand upon metal coordination. The bands in the range 500–615 cm^{-1} for all compounds are assigned to Ni-O bonds, thus confirming ligand coordination to the nickel center [39]. The NO_3 groups are coordinated to nickel ions in a monodentate fashion and exhibit absorption features at 1379 cm^{-1} for **3**, 1377 cm^{-1} for **4**, 1397 cm^{-1} for **5**, 1381 cm^{-1} for **6**, and 1384 cm^{-1} for **7** [40].

4.6. UV–Visible studies

The UV–Visible spectra of compounds **2**–**8** were recorded in methanol. All spectra exhibit well-defined broad bands in the low energy region, attributed to the $^3A_{2g}\rightarrow{}^3T_{2g}$, $^3A_{2g}\rightarrow{}^3T_{1g}(P)$, and $^3A_{2g}\rightarrow{}^3T_{1g}(F)$, as reported in the literature [41,42]. The bands in that region are shown in Table 10S for compounds **2**–**7** with the corresponding ε values. In compound **2**, the spectrum exhibits peaks at λ_{max} 1002 (ε 9.1 $M^{-1}\bullet cm^{-1}$), 606 nm (ε 5.2 $M^{-1}\bullet cm^{-1}$), with a weak low energy feature at 750 nm, and a distant band at 382 nm (ε 8.9 $M^{-1}\bullet cm^{-1}$) rising into the UV. The absorption feature around 385 nm could be tentatively attributed to the $^3A_{2g}\rightarrow{}^3T_{1g}(P)$ transition. The observed, seemingly "multiple" structure containing the 606 and 750 nm features, a region normally corresponding to the $^3A_{2g}\rightarrow{}^3T_{1g}(F)$ transition, is in line with literature reports invoking the presence of an ^1E_g state lying so close to $^3T_{2g}$ that extensive mixing takes place. That mixing leads to the observation of a "doublet" band, where the spin forbidden transition picks up intensity from the spin-allowed transition, thus accounting for the asymmetric complexity of the spectrum in that specific region [43]. Absorption features in the UV region at 300 and 302 nm could be attributed to LMCT processes. The aforementioned features are shown in Fig. 11S, exhibiting both the experimental and fitting spectra for **2**. In the ternary compound **3** (Fig. 13), the spectrum exhibits peaks at λ_{max} 962 (ε 8.5 $M^{-1}\bullet cm^{-1}$), 580 nm (ε 5.7 $M^{-1}\bullet cm^{-1}$), and a distant band at 342 nm (ε 105.9 $M^{-1}\bullet cm^{-1}$) rising into the UV. The absorption feature around 342 nm could be tentatively attributed to the $^3A_{2g}\rightarrow{}^3T_{1g}(P)$ transition. Absorption features at 305, 296, 244, and 202 nm could be attributed to LMCT and $\pi\rightarrow\pi^*$ transitions associated with the bound bipy ligand. In the ternary compound **4** (Fig. 12S), the spectrum exhibits peaks at λ_{max} 960 (ε 10.5 $M^{-1}\bullet cm^{-1}$), and 582 nm (ε 10.0 $M^{-1}\bullet cm^{-1}$). Distant bands at 290, 268, 222, and 202 nm could be attributed to LMCT and $\pi\rightarrow\pi^*$ transitions associated with the bound phen ligand. In the ternary compound **5** (Fig. 13S), the spectrum exhibits peaks at λ_{max} 982 (ε 6.7 $M^{-1}\bullet cm^{-1}$), 614 nm (ε 6.1 $M^{-1}\bullet cm^{-1}$), and a distant band at 341 nm (ε 57.6 $M^{-1}\bullet cm^{-1}$) rising into the UV. The absorption feature around 341 nm could be tentatively attributed to the $^3A_{2g}\rightarrow{}^3T_{1g}(P)$ transition. Absorption features at 305, 296, 243, and 202 nm could be attributed to LMCT and $\pi\rightarrow\pi^*$ transitions associated with the bound bipy ligand. In the congener compound **6** (Fig. 14S), the spectrum exhibits peaks at λ_{max} 921 (ε 8.4 $M^{-1}\bullet cm^{-1}$), 562 nm (ε 5.4 $M^{-1}\bullet cm^{-1}$), and a distant band at 341 nm (ε 655.7 $M^{-1}\bullet cm^{-1}$) rising into the UV. The absorption feature around 341 nm could be tentatively attributed to the $^3A_{2g}\rightarrow{}^3T_{1g}(P)$ transition. Distant absorption features at 269, 224, and 205 nm could be attributed to LMCT and $\pi\rightarrow\pi^*$ transitions associated with the bound phen ligand. By analogy, in the congener species **7** (Fig. 15S), the spectrum exhibits peaks at λ_{max} 855 (ε 4.2 $M^{-1}\bullet cm^{-1}$), 526 nm (ε 7.0 $M^{-1}\bullet cm^{-1}$), and a distant band at 342 nm (ε 846 $M^{-1}\bullet cm^{-1}$) rising into the UV. The absorption feature around 342 nm could be tentatively attributed to the $^3A_{2g}\rightarrow{}^3T_{1g}(P)$ transition. Distant absorption features at 269, 225, and 205 nm could be attributed to LMCT and $\pi\rightarrow\pi^*$ transitions associated with the bound phen ligand. The spectrum of compound **8** (Fig. 16S) exhibits features relevant to the overlapping presence of the hexaaqua complex $[Ni(H_2O)_6]^{2+}$ and the phen-containing species $[Ni(C_{12}H_8N_2)_3]^{2+}$. Due to the concurrent presence of both species in solution, no further attempts were made for spectral assignments of the individual species contributions to the composite UV-Visible signature. All of the aforementioned features of **2**–**8** are provided in the experimental spectra and supplemented by fitting spectral features. The spectra recorded for all compounds studied herein bear similar features to those of $[Ni(L)_6]^{2+}$ (L = H_2O, NH_3) ion, signifying the effect of the O,*N*-containing ligands on the electronic structure of Ni(II).

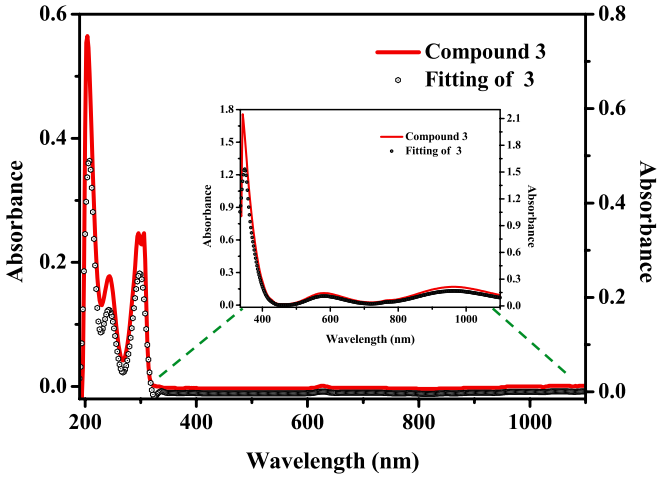

Fig. 13. UV–Visible (red line) and spectral fitting (circles) of compound **3** in methanol ($2.0 \cdot 10^{-5}$ M). **Inset:** Spectra of **3** in methanol ($2.0 \cdot 10^{-2}$ M) with fitting. ((Colour online.))

4.7. Luminescence studies

The luminescence properties of compounds **2**–**8** as well as those of pure free ligands Imino, bipy and phen were studied in the solid-state at 25 °C. Compounds **2** and **4** exhibit less intense bands (**Fig. 17SA**) at 419 nm (λ_{ex} = 380 nm) for **2**, and 420 nm (λ_{ex} = 381 nm) for **4**, compared to that of free phen ligand at 417 (λ_{ex} = 368 nm). The binary (**5**) and ternary (**3**) systems with the bipy ligand, as shown in **Fig. 17SB**, exhibit two lower intensity bands (compared to that of the ligand) at 385 nm, 398 nm (λ_{ex} = 342 nm) for **3** and two lower intensity bands shifted to 420 nm, 437 nm (λ_{ex} = 379 nm) for **5** in comparison to the bipy ligand (388 nm, λ_{ex} = 322 nm). Finally, the three different binary systems Ni-phen (**6**, **7**, **8**), in comparison to phen 417 (λ_{ex} = 368 nm), show a pattern of strong quenching at 421 nm (λ_{ex} = 382 nm) for **6**, 421 nm (λ_{ex} = 376 nm) for **7**, and 421 nm (λ_{ex} = 380 nm) for **8**, as illustrated in **Fig. 17SC**. The observed behavior may be attributed to the coordination of both the Imino, bipy and phen ligands to Ni(II) and is minimally affected by the presence of the coordinated aromatic chelator (bipy or phen) [44–46].

4.8. Magnetic susceptibility studies

Magnetic susceptibility measurements on all investigated compounds **2**–**7** show that the materials exhibit Curie-Weiss type paramagnetism (Fig. 14). The corresponding fitting parameters are summarized in Table 3. The experimentally derived magnetic moments range from 2.78 to 3.20 μ_B and thus slightly deviate from the theoretical moment of 2.83 μ_B for a Ni(II) ion in octahedral coordination [12]. There is almost no magnetic exchange observed in the paramagnetic regime. The Weiss constants θ_p have very low values and range from –1.9 to 0.6 K. Low-field data (inserts of Fig. 14, top) gave no evidence of magnetic ordering.

The 3 K magnetization isotherms show a continuous, field-induced increase of the magnetization and tendency toward saturation at 60 kOe, with magnetization values ranging from 1.61 to 2.04 μ_B. Thus, higher field strengths are necessary for full parallel spin alignment.

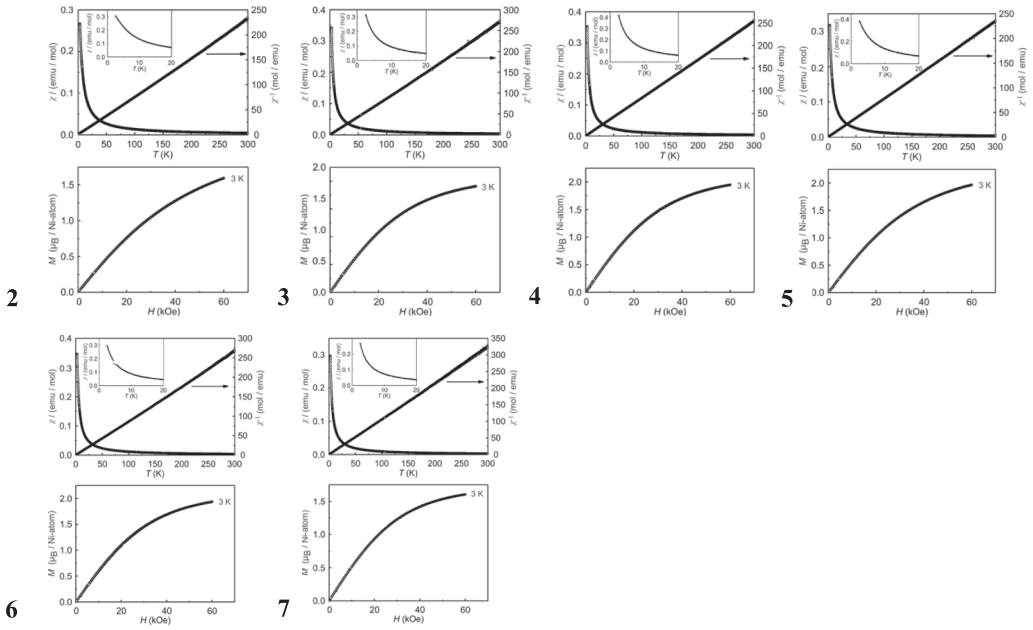

Fig. 14. Magnetic properties of compounds **2**–**7**: (top) Temperature dependence of the magnetic susceptibility and its inverse (χ and χ^{-1} data) recorded with an external field of 1 kOe; the inset shows the magnetic susceptibility in field-cooled (ZFC) mode at 20 Oe (**2**,**3**,**5**) and 50 Oe (**4**,**6**,**7**); (bottom) magnetization isotherms recorded at 3 K.

Table 3
Magnetic properties of compounds **2**–**7**, with μ_{eff}, effective magnetic moment, μ_{calc}, calculated magnetic moment, θ_p, paramagnetic Curie temperature, and μ_{sat} saturation moment values tabulated.

Compound	μ_{eff} / μ_B	$\mu_{eff,,theo}$ / μ_B	θ_P / K	μ_{sat} / μ_B
2	3.32(1)	2.83	–1.9(1)	1.60(1)
3	3.09(1)	2.83	–0.9(1)	1.92(1)
4	3.12(1)	2.83	–1.5(1)	1.95(1)
5	3.24(1)	2.83	–1.0(1)	1.97(1)
6	3.10(1)	2.83	–1.2(1)	1.94(1)
7	2.78(2)	2.83	–0.7(1)	1.61(1)

5. Discussion

5.1. Structural speciation and chemical reactivity

Comprehending chemical reactivity in a binary or ternary metal ion-containing system, in the presence of (O_n,N_m)-containing organic ligands, rides heavily and often decisively on the evolving structural speciation of the system investigated. In the case of the Ni(II) ion, the herein undertaken effort involved the a) employment of the imino dialcohol ligand (Imino), and ancillary aromatic chelators 2,2′-bipy and 1,10-phenanthroline, competing for positions in the coordination sphere of Ni(II). In an initial effort to pursue a binary complex assembly, selected reaction conditions led to a surprising isolation of two compounds of the same complex assembly $[Ni(C_6H_{15}NO_2)_2]^{2+}$, counterbalanced by nitrate ions originating in the starting material Ni$(NO_3)_2{\cdot}6H_2O$. To that end, **1** contains acetonitrile and water molecules in the lattice architecture, whereas **2** is devoid of any solvent in the architecture of the solid-state lattice. Distinctly differentiated, therefore, the Ni(II) cationic assembly in compound **1** contains the two Imino ligands appropriately fitting into the coordination sphere of Ni(II) so that the orientation of the sp^3 nitrogen Lewis bases occupy the two trans positions in the generated octahedron. In the cationic assembly of **2**, the nitrogens of the two Imino ligands occupy positions placing them in a cis configuration.

In a logically ensuing step in the chemical reactivity of the binary system toward a ternary system incorporating both the Imino and an aromatic chelator, such as bipy or phen, into the coordination sphere of Ni(II), appropriately selected reaction conditions afforded crystalline materials **3** and **4** from alcoholic media. X-ray crystallographic determination showed that the mixed ligand system had given rise to cationic assemblies $[Ni(C_6H_{15}NO_2)(C_{10}H_8N_2)(NO_3)]^+$ **3** (bipy) and $[Ni(C_6H_{15}NO_2)(C_{12}H_8N_2)(NO_3)]^+$ **4** (phen), respectively.

Delving further into the chemical reactivity of Ni(II) toward the Imino and bidentate aromatic chelators bipy and phen in CH_3CN, introduction of bipy led to the isolation of a crystalline material containing the cationic $[Ni(C_{10}H_8N_2)(NO_3)(CH_3CN)(H_2O)_2]^+$ assembly in **5**. Similar synthetic reactivity in water had previously led to the isolation of $[Ni(C_{10}H_8N_2)(NO_3)(H_2O)_3](NO_3)$, thus exemplifying the diversity of the coordination sphere of Ni(II) in different solvent systems as well as the related structural speciation [47]. By analogy to the reactivity leading to **5**, reaction of Ni(II) in the presence of phen in CH_3OH led to two crystallographically differentiated similar complex assemblies in $[Ni(C_{12}H_8N_2)_2(NO_3)(CH_3OH)]^+$ (compounds **6** and **7**). The two species (polymorphs) crystallized in the triclinic (**6**) and monoclinic (**7**) systems, respectively, thereby emphasizing the importance of reaction conditions in the isolation of the final product. The wealth of reactivity patterns and diversity of structural speciation associated with the solvent and ligand conditions employed with Ni(II) has so far produced analogous complex assemblies, with the solvent being predominantly encountered in the octahedral coordination sphere of Ni(II) in different numbers. Examples of such species include among others, $[Ni(C_{12}H_8N_2)(H_2O)_4](NO_3)_2{\bullet}H_2O$, $[Ni(C_{12}H_8N_2)_3](NO_3)_2{\bullet}4H_2O$, and $[Ni(C_{12}H_8N_2)_3]{\bullet}NiCl_4$ [48,49]. Finally, switching from alcoholic media to acetonitrile and in the presence of Ni(II):phen molecular stoichiometry 1:2, a crystalline material was isolated containing co-crystallized species in $\{[Ni(C_{12}H_8N_2)_3]_2[Ni(H_2O)_6]\}(NO_3)_6 \bullet 4CH_3CN{\bullet}H_2O$ (**8**). The heterogeneous nature of the complexes in the crystal structure of **8** exemplifies clearly the diversity of species coexisting under the described reaction conditions [50], which under appropriately employed "environmental pressure" (layering with ether) provide differential solubility conditions such that co-crystallization takes place. Surprisingly, again, the molar stoichiometry of $Ni(NO_3)_2$:phen in the original reaction mixture is the same as that encountered in compound **8**.

In all of the above cases, crystalline materials **1**–**8** were characterized

in the solid state and in solution, through analytical (elemental analysis), spectroscopic (FT-IR, UV–Visible, luminescence) and crystallographic techniques (X-ray diffractometry). Magnetic susceptibility studies **1**–**7** in the temperature range from 2.5 to 300 K, revealed a) behavior consistent with the mononuclear assembly of all complexes exhibiting Curie-Weiss type paramagnetism, and b) no evidence of magnetic ordering. The ensuing magnetization measurements at 3 K exhibit field-induced magnetization increase, with the numerical data suggesting that high field strength is required to achieve full parallel spin alignment. The collective spectroscopic and magnetic data are in line with the crystallographic data on both binary and ternary species of Ni(II).

Theoretical work (Hirshfeld, Electrostatic potential) on all species, relevant to their composition, assembly, and lattice properties, reflected intramolecular and intermolecular interactions emanating from the coordination of the respective ligands (organic and inorganic) as well as the counter ions and solvent molecules (e.g·H_2O, CH_3CN, CH_3OH). Furthermore, the electrostatic potential surface analysis and charge distributions on the generated molecular surfaces provided a detailed picture of each molecular assembly, when aromatic ring hydrophobicity enmeshes with the hydrophilicity of the Imino alcoholic oxygen anchors and contribute along with their bulk to the diverse picture of interactions in the collective picture of the molecules. In that respect, bound water and nitrato anion ligands along with the terminal Imino alcoholic groups contribute to their formulation as “acceptors”, bearing negative electrostatic potential, with the bound bulky aromatic chelators and the main body of Imino contributing to their “donor” profile, linked to positive electrostatic potential distributions.

Further electronic modeling of the emerging binary and ternary species through DFT calculations revealed the significant contributions of energetics into the observed chemical reactivity of the discrete complex Ni(II) assemblies. Comparative energy calculations among all species led to a rationalized arrangement of their structural-chemical behavior, consistent with the a) synthesis and isolation of conformational variants of the same species, and b) transformation reactions working from one species to another, yet not necessarily in both directions (vide infra). The overall experimental and theoretical work suggests that the chemical reactivity of the different aromatic binders with the ligand (Imino) and Ni(II) is key to the isolation of crystalline materials **1**–**8**.

5.2. Chemical transformations enrich speciation interconnectivity

To consolidate the importance of structural speciation in the establishment of a well-defined chemical reactivity profile for Ni(II) in binary and ternary systems, transformations were pursued to investigate potential interconnections between and among species originally synthesized from the simple starting materials (vide supra). To that end, compound $[Ni(C_6H_{15}NO_2)_2](NO_3)_2$ (**2**) reacted in methanol with bipy (1:1), ultimately affording $[Ni(C_6H_{15}NO_2)(C_{10}H_8N_2)(NO_3)](NO_3) \bullet 0.25\ CH_3OH$ (**3**). The invoked reactivity showed that the directly synthesized and isolated species could also form and be isolated through sequential formation of the binary species followed by replacement of one of the Imino ligands by the aforementioned aromatic chelator.

By the same token, reaction between $[Ni(C_6H_{15}NO_2)_2](NO_3)_2$ (**2**) and phen (1:1) in methanol, led to $[Ni(C_6H_{15}NO_2)(C_{12}H_8N_2)(NO_3)](NO_3) \bullet CH_3OH$ (**4**). The reaction suggests that the newly generated species is quite stable and can be synthesized from the initial binary system.

Further attempts to pursue complete replacement of both Imino ligands from the coordination sphere of Ni(II) in **2** were not successful. To that end, reaction of **2** with two equivalents of phen afforded **4**, with the fully replaced complex, purported to contain only phen, not having been isolated (under variable solvent, temperature, and stoichiometry conditions).

Transformation of the generated compounds a) $[Ni(C_{10}H_8N_2)(NO_3)(CH_3CN)(H_2O)_2](NO_3)$ (**5**), containing one bipy bound to Ni(II), b) $[Ni(C_{12}H_8N_2)_2(NO_3)(CH_3OH)](NO_3)$ (**6**) or $[Ni(C_{12}H_8N_2)_2(NO_3)(CH_3OH)](NO_3)$ (**7**), containing two phen ligands bound to Ni(II), and c) $\{[Ni(C_{12}H_8N_2)_3]_2[Ni(H_2O)_6]\}(NO_3)_6 \bullet 4CH_3CN \bullet H_2O$ (**8**), containing three phen ligands around Ni(II), with the Imino ligand, would be expected to lead to compound **3** or **4**. No such complexes, however, were isolated (under the present experimental conditions). By analogy, attempts to pursue transformation of the fully replaced phen and bipy-containing Ni(II) complexes with the Imino ligand-containing complex **2** were unsuccessful as well. Therefore, there are pieces of evidence defining the extent to which the reactivity of one system works toward the direction of another (containing new complex species), with the reverse process not affording **1**–**4**. Based on these results, a theoretical investigation was deemed appropriate and launched involving species **2**, **3**, and **4**.

Comparative computational analysis on **1** and **2**, as well as complex assemblies in **3**, **4**, **6** and **7**, revealed a discrete energy profile between **1** and **2**, clarifying their normalized formation energy with respect to each another (Fig. 12). For the ternary complex assemblies of the basic [Ni(Imino)] unit with phen/ bipy as well as their congener species, a well-defined energy profile was revealed for each one of them and moreover between them and structurally related complexes, essentially justifying the reasons for which the already tried chemical transformations experimentally worked well, whereas others (such as the transformation from the ternary Ni(II) species (**3**,**4**) back to the binary Ni(II) species **1** and **2** (removal of the aromatic chelator) or forward to binary species **5**–**7** (removal of the Imino ligand)) did not produce the envisioned products. Consequently, the electronic structure calculations provided a clear picture of the investigated chemical reactivity profile, thereby supporting the experimental work and laying the ground for new research into the specific chemistry.

6. Conclusions

The herein undertaken work investigated in depth the reactivity patterns of Ni(II) with a mixed (O,O,N) tridentate aliphatic organic ligand in the absence-presence of bidentate aromatic chelators bipy and phen. The rationally designed systems in organic solvent media, afforded binary and ternary crystalline materials, a) exhibiting octahedral coordination around Ni(II) in variable conformational states (**1** and **2**), b) projecting ternary mixed-ligand coordination environments around Ni(II), with the aromatic chelator forcing additional introduction of solvent and water molecules as ligands in the coordination sphere of the metal ion (**3** and **4**), and c) displaying diverse structural speciation of Ni(II)-bipy and Ni(II)-phen binary systems with a variable number of aromatic chelators present around Ni(II) (**5**–**8**). All species isolated were analytically, spectroscopically, magnetically, and structurally characterized, thus portraying the well-defined nature of the structural speciation in the investigated system and providing grounds for further inquiry into transformation chemistry, which interconnects structural participants and provides alternate ways of their synthesis in the arising reactivity pathways perused. The species transformation chemistry suggests that replacement of the Imino ligand does not proceed to full extent, thereby setting limitations in the synthetic reactivity among the various binary and ternary species studied. The reasons for such a selective reactivity pattern were sought through theoretical investigations so as to rationalize the differential stability and energetically discrete nature of the complexes made, in view of their chemical propensity toward the specific chelators. The physicochemical properties of binary and ternary species **1**–**8** define their corresponding profile through a plethora of techniques from elemental analysis to X-ray and magnetic susceptibility studies. Through such parameterized profiles, the distinct reactivity patterns of each species are well-described, thereby justifying global understanding of the structural speciation, which in turn lays the foundations for use of such compounds as precursors to new Ni(II) materials.

Declaration of Competing Interest

The authors declare that they have no known competing financial interests or personal relationships that could have appeared to influence the work reported in this paper.

Acknowledgements

This research was supported by the State Scholarships Foundation (IKY) for the doctoral scholarship co-financed by Greece and the European Union (European Social Fund - ESF) through the Operational Program "Human Resources Development, Education and Lifelong Learning" (NSRF 2014-2020), Act: "Strengthening the Human Research Resources through the Implementation of Doctoral Research" - MIS 5000432.

Appendix A. Supplementary data

CCDC 2077234 (**1**), 2077235 (**2**), 2077236 (**3**), 2077237 (**4**), 2077238 (**5**), 2077239 (**6**), 2077240 (**7**), 2077241 (**8**) contain the supplementary crystallographic data for this paper and have been deposited with the CCDC database. These data can be obtained free of charge via www.ccdc.cam.ac.uk/data_request/cif, or by emailing to data_request@ccdc.cam.ac.uk, or by contacting The Cambridge Crystallographic Data Centre, 12 Union Road, Cambridge CB2 1EZ, UK; Fax: +44 1223336033; or e-mail: deposit@ccdc.cam.ac.uk. Supplementary data to this article can be found online at https://doi.org/10.1016/j.poly.2021.115577.

References

[1] R. Patra, H.M. Titi, I. Goldberg, Cryst. Eng. Comm 15 (2013) 2853–2862, https://doi.org/10.1039/C3CE27006H.
[2] Y. Wei, Y. Yu, R. Sa, Q. Li, K. Wu, Cryst. Eng. Comm. 11 (2009) 1054–1060, https://doi.org/10.1039/B815464C.
[3] V.A. Neacşu, C. Maxim, A.M. Mădălan, M. Hillebrand, C. González-Arellano, S. Soriano, E. Rentschler, M. Andruh, Polyhedron 150 (2018) 77–82, https://doi.org/10.1016/j.poly.2018.05.007.
[4] P. Gikas, J. Hazard. Mater. 159 (2008) 187–203, https://doi.org/10.1016/j.jhazmat.2008.02.048.
[5] G. Zamborlini, M. Jugovac, A. Cossaro, A. Verdini, L. Floreano, D. Lüftner, P. Puschnig, V. Feyer, C.M. Schneider, Chem. Comm. (Cambridge England) 54 (2018) 13423–13426, https://doi.org/10.1039/C8CC06739B.
[6] K.C. Chan Chung, D.B. Zamble, J. Biol. Chem. 286 (2011) 43081–43090, https://doi.org/10.1074/jbc.M111.290726.
[7] J.M. Ramos, O. Versiane, J. Felcman, Spectrochim. Acta A: Molecular and Biomolecular Spectroscopy 72 (2009) 182–189, https://doi.org/10.1016/j.saa.2008.09.026.
[8] U. Ermler, W. Grabarse, S. Shima, M. Goubeaud, R.K. Thauer, Curr. Opin. Struct. Biol. 8 (1998) 749–758, https://doi.org/10.1016/S0959-440X(98)80095-X.
[9] R. Chakrabarty, P.S. Mukherjee, P.J. Stang, Chem. Rev. 111 (2011) 6810–6918, https://doi.org/10.1021/cr200077m.
[10] R.-Y. Li, Z.-M. Wang, S. Gao, Cryst. Eng. Comm. 11 (2009) 2096–2101, https://doi.org/10.1039/B906694M.
[11] C. Wei, Y. He, X. Shi, Z. Song, Coord. Chem. Rev. 385 (2019) 1–19, https://doi.org/10.1016/j.ccr.2019.01.005.
[12] H. Lueken, Magnetochemistry, Compounds and Concepts, Teubner, Stuttgart, 1999.
[13] G.A. Bain, J.F. Berry, J. Chem. Educ. 85 (2008) 532–536, https://doi.org/10.1021/ed085p532.
[14] K. Momma, F. Izumi, J. Appl. Cryst. 44 (2011) 1272–1276, https://doi.org/10.1107/S0021889811038970.
[15] I.D. Brown, D. Altermatt, Acta. Cryst. B 41 (1985) 244–247, https://doi.org/10.1107/S0108768185002063.
[16] W. Liu, H.H. Thorp, Inorg. Chem. 32 (1993) 4102–4105, https://doi.org/10.1021/ic00071a023.
[17] M.A. Spackman, D. Jayatilaka, Cryst. Eng. Comm. 11 (2009) 19–32, https://doi.org/10.1039/B818330A.
[18] F.L. Hirshfeld, Theor. Chim. Acta 44 (1977) 129–138, https://doi.org/10.1007/BF00549096.
[19] H.F. Clausen, M.S. Chevallier, M.A. Spackman, B.B. Iversen, New J. Chem. 34 (2010) 193–199, https://doi.org/10.1039/B9NJ00463G.
[20] M.A. Spackman, J.J. McKinnon, Cryst. Eng. Comm. 4 (2002) 378–392, https://doi.org/10.1039/B203191B.
[21] A. Parkin, G. Barr, W. Dong, C.J. Gilmore, D. Jayatilaka, J.J. McKinnon, M. A. Spackman, C.C. Wilson, Cryst. Eng. Comm. 9 (2007) 648–652, https://doi.org/10.1039/B704177B.
[22] A.L. Rohl, M. Moret, W. Kaminsky, K. Claborn, J.J. McKinnon, B. Kahr, Cryst. Growth Des. 8 (2008) 4517–4525, https://doi.org/10.1021/cg8005212.
[23] M.J. Turner, J.J. McKinnon, S.K. Wolff, D.J. Grimwood, P.R. Spackman, D. Jayatilaka, M.A. Spackman, Crystal Explorer 17.5, The University of Western Australia, 2017.
[24] F.H. Allen, O. Kennard, D.G. Watson, L. Brammer, A. Guy Orpen, R. Taylor, J. Chem. Soc. Perkin Trans. 2 (1987) S1–S19, https://doi.org/10.1039/P298700000S1.
[25] I.D. Madura, J. Zachara, H. Hajmowicz, L. Synoradzki, J. Mol. Struct. 1017 (2012) 98–105, https://doi.org/10.1016/j.molstruc.2012.02.053.
[26] V. Rajni Swamy, C. Ravikumar, J. Mol. Struct. 1225 (2021) 129313, https://doi.org/10.1016/j.molstruc.2020.129313.
[27] S.L. Tan, M.M. Jotanib, E.R.T. Tiekinka, Acta Cryst. E 75 (2019) 308–318, https://doi.org/10.1107/S2056989019001129.
[28] G. Kresse, J. Furthmüller, Phys. Rev. B 54 (1996) 11169–11186, https://doi.org/10.1103/PhysRevB.54.11169.
[29] J.P. Perdew, K. Burke, M. Ernzerhof, Phys. Rev. Lett. 78 (1997) 1396, https://doi.org/10.1103/PhysRevLett.78.1396.
[30] Bruker Analytical X-ray Systems, Inc. Apex2, Version 2 User Manual, M86-E01078, Madison, WI, 2006.
[31] Siemens Industrial Automation, Inc. SADABS: Area-Detector Absorption Correction, Madison, WI, 1996.
[32] P.W. Betteridge, J.R. Carruthers, R.I. Cooper, K. Prout, D.J. Watkin, J. Appl. Cryst. 36 (2003) 1487, https://doi.org/10.1107/S0021889803021800.
[33] L. Palatinus, G.J. Chapuis, Appl. Cryst. 40 (2007) 786–790, https://doi.org/10.1107/S0021889807029238.
[34] D.J. Watkin, C.K. Prout, L.J. Pearce, CAMERON, Chemical Crystallography Laboratory, Oxford, UK, 1996.
[35] DIAMOND – Crystal and Molecular Structure Visualization, Ver. 3.1c, Crystal Impact, Bonn, Germany, 2006.
[36] W.M.I. Hassan, M.A. Badawy, G.G. Mohamed, H. Moustafa, S. Elramly, Spectrochim. Acta 111 (2013) 169–177, https://doi.org/10.1016/j.saa.2013.03.085.
[37] M.M. Campos-Vallette, R.E. Clavijo, F. Mendizabal, W. Zmudio, R. Baraona, G. Diaz, Vibrational Spectroscopy 12 (1996) 37–44, https://doi.org/10.1016/0924-2031(96)00012-4.
[38] A. Rujiwatra, S. Yimklan, T.J. Prior, Polyhedron 31 (2012) 345–351, https://doi.org/10.1016/j.poly.2011.09.046.
[39] Y. Xiao, Y. Qin, M. Yi, Y. Zhu, J. Clust. Sci. 27 (2016) 2013–2023, https://doi.org/10.1007/s10876-016-1059-y.
[40] K. Nakamoto, Infrared and Raman Spectra of Inorganic and Coordination Compounds Part A: Theory and Applications in Inorganic Chemistry, 6th Edition, John Wiley & Sons, New Jersey, 2009.
[41] R.S. Drago, in: Physical Methods in Chemistry, W.B. Saunders Company, Philadelphia, 1977, pp. 359–410.
[42] M. Menelaou, M. Dakanali, C.P. Raptopoulou, C. Drouza, N. Lalioti, A. Salifoglou, Polyhedron 28 (2009) 3331–3339, https://doi.org/10.1016/j.poly.2009.05.084.
[43] A.B.P. Lever, in: Inorganic Electronic Spectroscopy, 2nd Edition, Elsevier, Amsterdam, 1984, pp. 507–511.
[44] D.A. Kara, A. Donmez, H. Karaa, M.B. Coban, Acta Cryst. C 74 (2018) 901–906, https://doi.org/10.1107/S2053229618009166.
[45] Q.-P. Kang, X.-Y. Li, Z.-L. Wei, Y. Zhang, W.-K. Dong, Polyhedron 165 (2019) 38–50, https://doi.org/10.1016/j.poly.2019.03.008.
[46] X.-X. An, Q. Zhao, H.-R. Mu, W.-K. Dong, Crystals 9 (2019) 101, https://doi.org/10.3390/cryst9020101.
[47] F. Walmsley, A. Pinkerton, J.A. Walmsley, Polyhedron 8 (1989) 689–693, https://doi.org/10.1016/S0277-5387(00)83832-2.
[48] M. Tabatabaee, N. Zaji, M. Parvez, Acta Cryst Sect E Struct. Rep. Online 67 (2011) m1794–1795, https://doi.org/10.1107/S160053681104880X.
[49] S.M. Khake, S. Jain, U.N. Patel, R.G. Gonnade, K. Vanka, B. Punji, Organometallics 37 (2018) 2037–2045, https://doi.org/10.1021/acs.organomet.8b00177.
[50] O. Yu. Kadnikova, Yu. A. Kondratenko, V.V. Gurzhiy, V.L. Ugolkov, T.A. Kochina, Russ. Chem. Bull., International Edition, 69(5) (2020) 958-964, https://doi.org/10.1007/s11172-020-2855-y.